

Preliminary and Detailed Design Report of a Regional Airliner Jet

Academic responsible: Dr. Errikos Levis & Dr. Yang Daqing
Department: Department of Aeronautics
Course: MEng in Aeronautics
Module: AERO60002
Academic year: 2022/2023
Student: Amelia Samuel - 01873907
Aryaa Desai - 01846886
Avish (Ave) Madhow - 01951532
Chris Ziyi Yao - 01908293
Stephen Cao - 01854692
YiChen You - 01863827
Group: 01
Date: 07/02/2023

Department of Aeronautics
South Kensington Campus
Imperial College London
London SW7 2AZ
U.K.



Abstract

This report describes the preliminary design phase of a 90-passenger regional jetliner. The structural layout of an aircraft during its conceptual design stage is analysed using developed airframe structural knowledge and engineering approximations as well as established methodology. The first iteration of the aircraft's structural layout is determined through analytical calculations, taking into account the Ultimate Limit Load of 3.75 as well as three different load cases, along with a review of similar aircraft and adherence to airworthiness regulations. The primary focus is on the fuselage, wings, and empennage. Material selection using CES was also conducted for these components. Secondary structures are also considered but have no numerical impact on the analysis. Following the preliminary state, the report describes the detailed design of a component of the aircraft's flap extension mechanism using Finite Element Analysis and optimisation techniques such as topology optimisation and generative design. This was conducted while ensuring the mass was optimised and performance metrics such as Ultimate Tensile Strength and buckling considerations were met.

Contents

List of Symbols	ii
List of Figures	v
List of Tables	vii
1 Introduction	1
2 Review of Similar Aircraft	2
2.1 Fuselage	2
2.1.1 Skin	2
2.1.2 Stringers	2
2.1.3 Frames	2
2.2 Wings	2
2.2.1 Wing Box (Spars)	2
2.2.2 Ribs	3
2.3 Comparison of Empennage with Similar Aircraft	3
3 Material Selection	3
3.1 Wings and Empennage	4
3.2 Fuselage	5
3.3 Summary of Material Selection	6
4 Wing Design	6
4.1 Design strategy	6
4.2 Load Modelling	6
4.3 Spar Design	8
4.3.1 Geometry and Assumptions	8
4.3.2 Sizing and Optimisation	9
4.4 Skin Stringer Panels Design	11
4.4.1 Geometry and Assumptions	11
4.4.2 Sizing and Optimisation	12
4.5 Rib Design	15
4.6 Geometry & Mass Summary	16
4.6.1 Geometry	16
4.6.2 Mass	16
4.6.3 Stress Ratio	16
5 Fuselage Design	17
5.1 Design Strategy	17
5.2 Load Cases	17
5.2.1 Mass Distribution	17
5.2.2 Load Case 1: Symmetric Loading at Ultimate Load Factor	18
5.2.3 Load Case 2: Asymmetric Loading at OEI	19
5.2.4 Load Case 3: Loading at Nose-off Landing	21
5.2.5 Maximum Loadings Summary	22
5.3 Pressure Loads	22
5.4 Stringer-Skin Design	23
5.4.1 Skin	23
5.4.2 Stringers	24
5.4.3 Verification of skin-stringer design	26
5.5 Light Frame Design	27
5.6 Heavy Frame Design	28
5.6.1 Tangential Load Case	28
5.6.2 Radial Load Case	28
5.6.3 Moment Load Case	28
5.6.4 Superposition of Cases	29

5.7	Mass Breakdown of Fuselage	31
6	Horizontal Stabiliser Design	31
6.1	Design Strategy	31
6.2	Load Cases	31
6.3	Spar Design	32
6.3.1	Geometry	32
6.3.2	Sizing and Optimisation	32
6.4	Skin Stringer Panels Design	34
6.5	Rib design	35
6.6	D - Cell section	36
6.7	Geometry & Mass Summary	36
7	Vertical Stabiliser Design	37
7.1	Design Rational	37
7.2	Material Selection	37
7.3	Load Considerations	38
7.4	Skin/Cover Design	39
7.4.1	Sizing Procedure	39
7.4.2	Buckling Analysis	40
7.5	Spar Design	41
7.6	Ribs Design	42
7.7	D-Section Design	42
7.8	Geometry & Mass Summary	43
8	Secondary Structures	44
8.1	Cut-Outs	44
8.2	Joints and Fittings	44
8.3	Engine Mount	44
8.4	Undercarriage	45
8.5	Leading and Trailing Edge Devices	45
9	Detailed Component Design	45
9.1	Objective	45
9.2	Design Approach and Selection of Final Design	45
9.3	Modelling Assumptions	48
9.4	Verification through Mesh Convergence	48
9.5	Topology Optimisation and Generative Design	48
10	Evaluation of Preliminary Design	49
10.1	Wing	49
10.2	Fuselage	50
10.3	Empennage	50

List of Symbols

A	Cross Sectional Area
b	Web Height
c	Cost, Sectional Chord
C_f	Empirical Constant
C_{M0}	Zero Moment Pitching Coefficient
D	Diameter
D_x	Negative First Moment of Area
d	Stringer Flange Width
E	Young's Modulus
F	Farah
F_{crush}	Crush Force
F_y	Vertical Force
G	Shear Strength
h	Web Height
I_x	Second Moment of Area
L	Rib Spacing, Length
M	Material Index
m_0	Zero-pitch moment
N	Tip, Compressive Load, Force per unit length
n	Number of plies
n_{LLF}	Limit Load Factor
n_{ULF}	Ultimate Load Factor
P	Pressure, Tangential Load
q	Shear flow
Q	Radial Load
R_c	Compressive Stress Ratio
R_s	Shear Stress Ratio
R_F	Front Spar Reaction Force
R_R	Rear Spar Reaction Force
S_f	Fatigue Strength
SF	Shear Force
T	Torque
T_{max}	Maximum Thrust
t	Thickness
V	Total Shear Flow
V_A	Maneuver Speed
V_D	Dive Speed
w	Weight Distribution
ρ	Density, Radius of Gyration
σ	Stress
ϵ_H	Hoop Strain
μ	Poisson Ratio
θ	Point Load Acting Angle
η	Merit Index

Subscript Meaning

2	Skin, Shear
c	Compressive
HT	Horizontal Tailplane
r	Ribs
s	Stringers
t	Tensile
VT	Vertical Tailplane
w	Wing
y	Yield

Common Terminology

BM	Bending Moment
SF	Shear Force
ETB	Engineer's Theory of Bending
HT	Horizontal Tailplane
OEI	One Enginer Inoperative
HT	Vertical Tailplane
MTOW	Maximum Take-Off Weight
MZFW	Maximum Zero Fuel Weight

List of Figures

1	n-V Diagram Showing Manoeuvring Loads	1
2	Typical Spar Configuration	3
3	Ashby Chart for $M_{upperwing}$ with Design Guideline Slope of 1	4
4	Ashby Chart for $M_{lowerwing}$ with Design Guideline Slope of 2	4
5	Ashby Chart for $M_{fuselage}$ with Design Guideline Slope of 1.5	5
6	Ashby Chart for $M_{fuselagframe}$ with Design Guideline Slope of 0.5	5
7	Graphs for load cases of wing	8
8	Shear Buckling Coefficient K_s Against the Aspect Ratio of a Plate under different Boundary Conditions [1]	9
9	Total Mass and the Estimated Cost of the Spars Against the No. of Stiffeners	10
10	Normalised Spar Mass of Front and Rear Spars Against Normalised Root Spar Thickness	10
11	Front and Rear Spar Thickness Distribution Along the Span	11
12	Spanwise Thickness Distribution with Manufacture Concerned	11
13	Farrar's Efficiency Factor (F) for Z-Stringer Panels [2]	12
14	K and $\frac{t_s}{t}$ Against $\frac{h}{b}$ for Z-Stringer Panels [3]	12
15	Total Mass of Stringer Panels of two Wings Varies with the No. of Panels	13
16	Total Mass Against Root Skin Thickness	13
17	Thickness and Height Distribution Along the Span	14
18	Modification with Clearance and Tolerance Concerns	14
19	Farrar Factor Distribution Along the Span	14
20	Stringer and Rib Weights VS. Rib Spacing	15
21	Stress Ratio Along the Span	16
22	Distributed Mass vs x-Positions from the Aircraft Nose	18
23	Load Case 1 Results	19
24	Load Case 2 OEI Moment Equilibrium (Drawn not to Scale)	20
25	Load Case 2 Results	21
26	Load Case 3 Results	22
27	Shear Flow Around Fuselage Skin	24
28	Relationships between area, mass and stringer number	24
29	Dimensional Constraints on Stringer Number	25
30	Boom Shear Idealisation and Shear Flow	25
31	Z-stringer Dimensions	26
32	Relationship Between Stress Ratio and Minimum Stringer Area Required	27
33	Relationship Between Thickness, Width, and Height of Fuselage Light Frame	27
34	Wise Plots	29
35	Heavy Frames	30
36	Location of all the Heavy Frames Along the Aircraft	31
37	Horizontal tail-plane loads	32
38	Total Mass and Cost of the Fin Spars Against the Numbers of the Stiffeners	33
39	Front and Rear Spar Thickness Distribution Along the Span	33
40	Spanwise Thickness Distribution with Manufacture Concerned	34
41	Total Mass and Cost Varies with the No. of Panels	34
42	Thickness and Height Distribution Along the Span	35
43	Modification with Clearance and Tolerance Concerns	35
44	Optimum rib Spacing for Main Wing box of Horizontal Tail-plane	36
45	Stress and Weight Analyses with Varying Numbers of Ribs	36
46	Ashby Chart for M_{Foam} With Design Guideline Slope of 2	38
47	Loads Evaluated in Load Case 2 (MTOW)	39
48	Varying Foam Thickness Spanwise to Increase Buckling Resistance	40
49	Spar Web Thickness Varying Along the Span of the Vertical Tail	41
50	Optimum Number of Spar Stiffeners Using Mass and Cost (in £) Constraints	41
51	Effect of Varying Rib Spacing on Weight	42
52	Spar Web Thickness Varying Along the Span of the Vertical Tail	43
53	Vertical Stabiliser Geometry	44
54	Engine Mount	45
55	Loading Effects on Engine	45

56	Iteration 1	46
57	Iteration 2	46
58	Stress Distribution of Iteration 1	46
59	Iteration 3	47
60	Iteration 4	47
61	Stress Distribution of Iteration 3	47
62	Final Iteration	47
63	Stress Distribution of Final Iteration	47
64	Final Iteration Deflection Magnitude	47
65	First Buckling mMode of Final Iteration	47
66	Topology Optimisation Stresses	49
67	Topology Optimisation Maximum Deflection	49
68	Generative Design Stresses	49
69	Generative Design Maximum Deflection	49
70	Uniaxial Load Combinations of Clamped and Simply-Supported Edge Conditions	53

List of Tables

1	Spar and Rib Configurations for the Horizontal Stabiliser of Similar Aircraft	3
2	Spar and Rib Configurations for the Vertical Stabiliser of Similar Aircraft	3
3	Material Properties of the Aluminium Alloys Chosen	6
4	Wingbox Geometry at the Root and the Tip of the Wing	9
5	Initial Sizing of the Spars at the Root and the Tip of the Wing	10
6	Wing Rib Geometry sample Summary with Rib Spacing of 0.4 m	16
7	Wing Spar Web Geometry at the Root	16
8	Mass Breakdown for the Wing Components	16
9	Fuselage Stringer-skin Design Variable Range[4]	17
10	Mass Distribution Type for Each Aircraft Component	18
11	Maximum Shear Force, Bending Moment, and Torque of Fuselage Loading Cases	22
12	Key Values and Dimensions for Pressure Sizing	23
13	Summary of Q, P and T Values for Load Case 1 and 2	23
14	Summary of the Chosen Dimensions for the Stringers	26
15	Light Frame Dimensions	28
16	Table displaying values of resolved tangential, radial and moment loads as well as radius and θ . The radius for the horizontal and vertical tailplanes was taken as an average of the radius of the fuselage at the front and rear spars of the component.	29
17	Summary of Minimum Areas Required to Resist Shear and Direct Stresses	30
18	Summary of Heavy Frame Dimensions	31
19	Mass breakdown of Fuselage	31
20	Finbox Geometry at the Root and the Tip	32
21	Initial Sizing of the Spars at the Root and the Tip of the Wing	32
22	Horizontal Tailplane Rib Geometry Summary with Rib Spacing of 1.5 m	36
23	Horizontal Tailplane Spar web Geometry at the Root	37
24	Mass Breakdown for the Horizontal Tailplane Components	37
25	Material Properties for Composite Design. † Tensile Modulus 0°, * In-plane $G_{12} = G_{31}$	38
26	Maximum Shear Force, Bending Moment and Torque on the Vertical Tail (at the Root)	39
27	Sandwich Composite Panel Summary With the Thickness Evaluated at the Root	43
28	Vertical Tailplane Rib Geometry Summary With Chosen rib Spacing of 1.5m	43
29	Spar web Geometry at the Root	43
30	Mass Breakdown for the Vertical Tailplane Components	43
31	Summary of Design Metrics	48
32	Mesh Convergence Study	48
33	Design Comparison	49

1 Introduction

This report describes the preliminary and detailed design stage of the passenger jet aircraft following the "Conceptual Design Report of a Regional Airliner Jet" [5]. An aircraft is subject to multiple loads within its flight envelope as highlighted in figure 1.

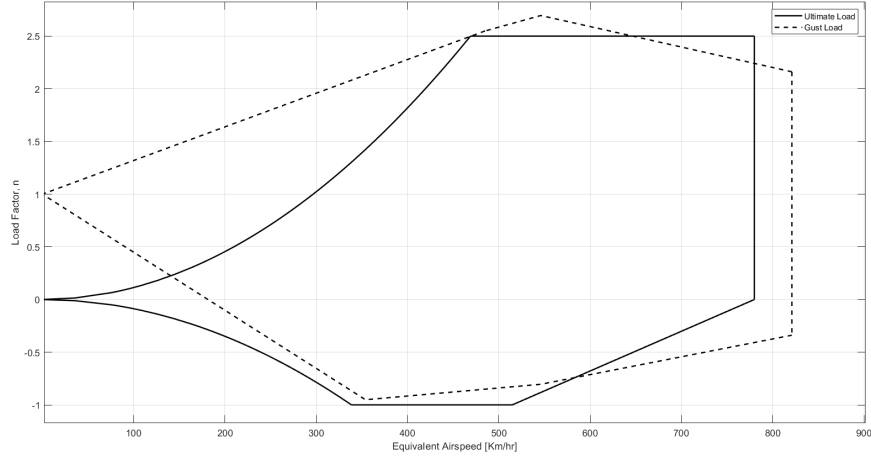


Figure 1: n-V Diagram Showing Manoeuvring Loads

The following load factors, n , are important design considerations:

Limit Load Factor, $n_{LLF} = 2.5$

This represents the maximum load that an aircraft is expected to experience in its service life.

Ultimate Load Factor, $n_{ULF} = 1.5 \cdot n_{LLF} = 3.75$

The limit load is multiplied by a safety factor of 1.5. The structure must be able to support the ultimate load before failure.

The structural components examined are the wings, fuselage, horizontal and vertical stabilisers, subject to the following load cases:

Load Case 1

Symmetric flight at n_{ULF} , evaluated at manoeuvre V_A and dive V_D speeds, to determine the structural loading of the wing, fuselage and tail structures at failure.

Load Case 2

One Engine Inoperative condition. Assume a load acting at the aerodynamic centre of the vertical stabiliser such that the aircraft is directionally trimmed in case of a single critical engine failure. This is an asymmetrical loading condition.

Load Case 3

Landing with the front nose-off case. Hence the full aircraft load is supported by the main undercarriage only. All aerodynamic loads may be ignored.

These load cases represent the extremes of the potential load cases. They are evaluated at the following aircraft design weights:

1. MTOW (Maximum Take-Off Weight)
2. MZFW (Maximum Zero Fuel Weight)

2 Review of Similar Aircraft

A review of similar aircraft served as a guide for the design decisions made in the preliminary design phase. Structural design is the main focus in the aerospace industry. The main structural components to be reviewed were the fuselage, the wing and the empennage.

2.1 Fuselage

The fuselage is the central body of the aircraft accommodating the crew, passengers and potential cargo. It serves as the structural connection for the wings and empennage.

2.1.1 Skin

Modern commercial aircraft have skins of either metal or composite. From the Conceptual Design stage [5], all-metal construction is selected for the jetliner. 2-series and 6-series Aluminium are very popular for Aerospace applications. Al 2024-T3 and Al 6082-T6. Aluminium-Lithium alloys are an appealing prospect due to their excellent mechanical properties and low weight. These alloys are however very expensive.

2.1.2 Stringers

For metallic structures, Z-stringers are typically used since they sustain the greatest load per unit weight and these types of stringers can be found on aircraft such as the Boeing 737 and 747. Composite stringer cross-sections usually have a "top hat" or omega cross-section, such as those seen on the A350, to leave no free edges. This inspects cracks extremely involved, thus making maintenance and repair very difficult and expensive.

2.1.3 Frames

Fuselage frames transfer loads to the fuselage shell and provide column support for the longitudinal stringers. The frames generally take the form of open rings, so that the interior of the fuselage is not obstructed. They are connected continuously around their peripheries to the fuselage shell and are not necessarily circular but usually symmetrical about a vertical axis. A fuselage frame is in equilibrium under the action of any external loads and the reaction shear flows from the fuselage shell [6]. Heavy frames are designed to be the main load-bearing structure for parts connected to the fuselage, namely wings and stabilisers. As such, heavy frames are only found where wing and stabiliser spars meet the fuselage and this layout for the heavy frames is standard in commercial aviation aircraft. Light frames, as opposed to heavy frames, are not primarily designed to carry loads: the main role of light frames is to prevent the skin from buckling. As such, all commercial aircraft tend to have light frame spacing of 0.5m, regardless of aircraft weight.

2.2 Wings

The wings are the main lifting surfaces with an aerofoil cross-section. The main structural components of the wing are the spars, ribs and stringers.

2.2.1 Wing Box (Spars)

Spars are heavy beams running spanwise to resist transverse shear loads and spanwise bending. Most modern commercial jetliners have two spars per wing. This configuration provides the structural integrity for a commercial aircraft to survive the worst possible scenario loads whilst keeping the weight low. Different spar beam constructions are shown in Figure 2. Spars can be divided into truss types or shear web types. Due to the relatively benign loads a commercial aircraft will experience, a built-up web design is selected which matches the industry standard.

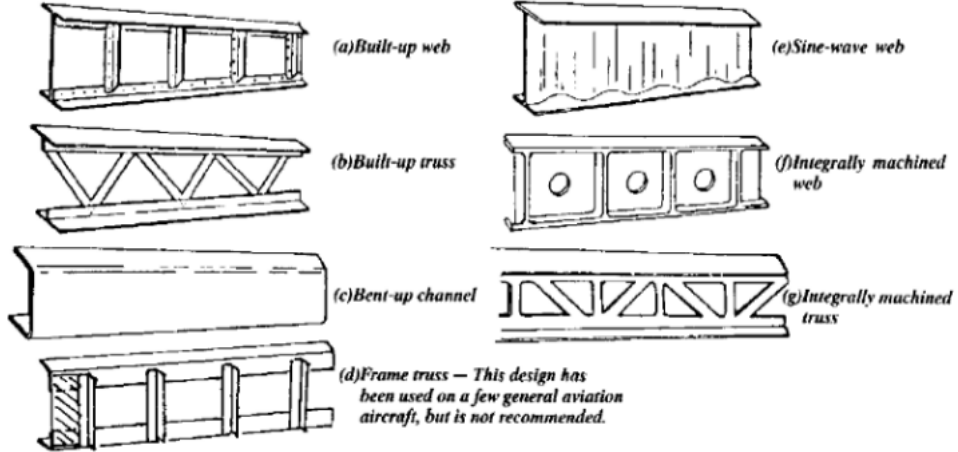


Figure 2: Typical Spar Configuration

2.2.2 Ribs

Ribs are structural crosspieces that combine with spars and stringers to make up the framework of the wing. They usually extend from the wing's leading edge to the rear spar or to the trailing edge of the wing. The ribs give the wing its cambered shape and transmit the load from the skin and stringers to the spars. Similar ribs are also used in ailerons, elevators, rudders, and stabilisers.

2.3 Comparison of Empennage with Similar Aircraft

The following tables compare the different parameters of the horizontal and vertical stabilisers for similar regional jetliners [7].

Table 1: Spar and Rib Configurations for the Horizontal Stabiliser of Similar Aircraft

Aircraft	ARJ-21	A320	A220-100	E-190
No. of Spars	3	2	4	3
No. of Ribs	14	24	28	23
Horizontal Stabiliser Semi-span (m)	6.50	3.90	5.23	4.57
MTOW (tonnes)	40.0	78.0	60.0	50.8

Table 2: Spar and Rib Configurations for the Vertical Stabiliser of Similar Aircraft

Aircraft	ARJ-21	A320	A220-100	E-190
No. of Spars	3	2	4	3
No. of Ribs	15	18	14	20
Vertical Stabiliser Semi-span (m)	3.50	3.87	3.83	3.80
MTOW (tonnes)	40.0	78.0	60.0	50.8

3 Material Selection

Since the aircraft acts as a commercial transport plane, the wrought aluminium alloy was selected due to its extensive use in aviation leading to a large catalogue of tested aerospace aluminium alloys with a range of mechanical properties, prices and densities. Aluminium alloys have a high specific strength, high corrosion resistance and good manufacturability were some of the major justifications for their use in lifting surfaces, fuselage and empennage. Using CES [8], material indices were created which allowed the most suitable aluminium alloys to be showcased. For all the materials the denominator contains the material density ρ and price c since the two parameters were the most important to minimise due to the aircraft's intended use while mechanical properties were to be maximised.

3.1 Wings and Empennage

The upper and lower skin of the wing has different materials as the wing experiences more bending due to aerodynamic loading than the fuselage and material failure on the wing is far more catastrophic than on the fuselage; Aloha Airlines Flight 243 landed successfully without part of the fuselage [Ref]. The upper surface undergoes cyclic compression loading while the lower surface experiences cyclic tension loading. The properties to be maximised were compression strength σ_c and tensile strength σ_t for the upper and lower surfaces respectively and fatigue strength S_f and torsional strength G for both surfaces resulting in the following material indices [8]:

$$M_{upperwing} = \frac{\sigma_c^{2/3} GS_f}{\rho c} \quad (1)$$

$$M_{lowerwing} = \frac{\sigma_t^{2/3} GS_f}{\rho c} \quad (2)$$

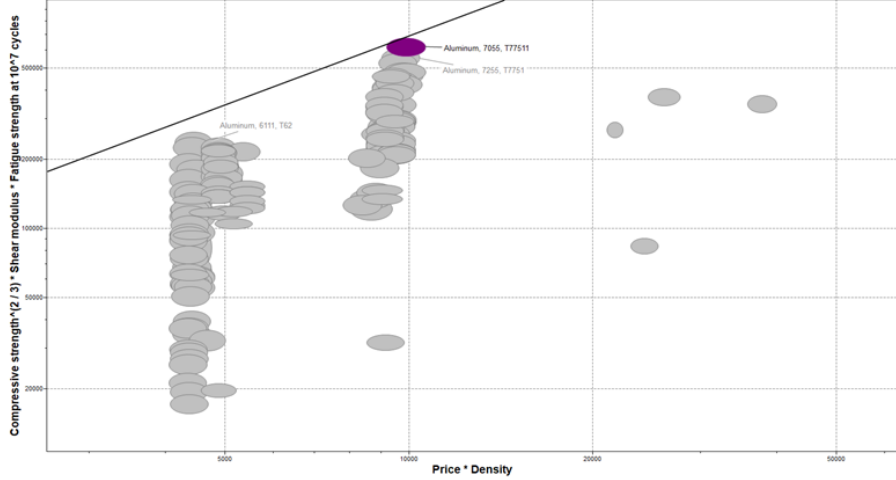


Figure 3: Ashby Chart for $M_{upperwing}$ with Design Guideline Slope of 1

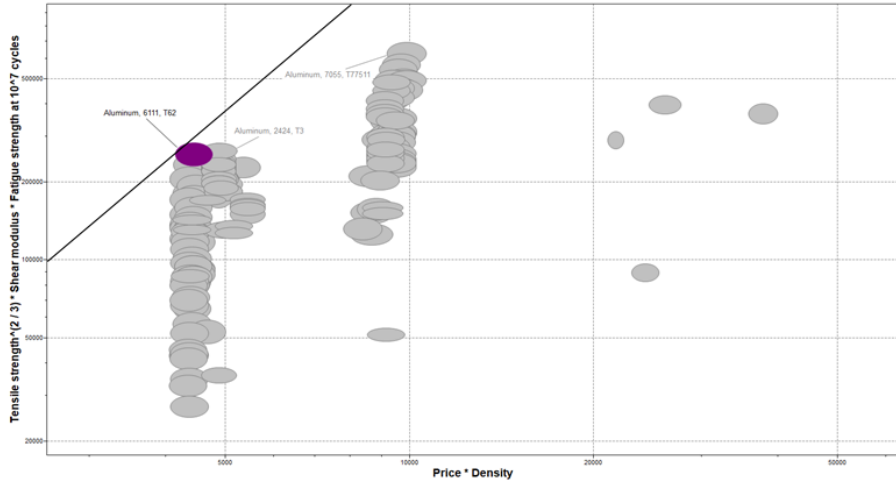


Figure 4: Ashby Chart for $M_{lowerwing}$ with Design Guideline Slope of 2

From Figure 3, it was clear that Aluminium 7055-T77511 was the optimal choice for the upper surface of the wing and Aluminium 6111-T62 was suitable for the lower wing surface displayed in Figure 4. Aluminium 6111-T62 also possessed good torsion, yield and compression strength characteristics to be utilised for the wings spar and rib material. Stringers are integrated into the wing surfaces and therefore have the same material properties. For the horizontal tailplane, it would use the same material choice as the wing while the vertical tailplane material choice and its design will be explored in Section 7

3.2 Fuselage

The fuselage experiences many loads, axial and shearing forces from bending of the upper and lower fuselage as well as cyclic pressure loads from cabin pressurisation. Bending of the fuselage will result in the lower skin experiencing tensile stresses while the upper skin experiences compression stresses. However, it was decided not to have the fuselage skin consist of two materials for the upper and lower fuselage as the joining running along the whole length of the cabin was a critical source of failure and heavy reinforcements of rivets, welding or adhesives would add weight as well as complexity since the two alloys may wear or deform at varying rates over different moisture and temperature ranges. Consequently, materials with good torsional G, tensile σ_t and compression σ_c strength as well as fatigue resistance S_f properties were chosen and maximised with the material indices shown in Equation 3. For the fuselage stringers, light and heavy frames' tensile and yield strength were chosen to be maximised as shown in Equation 4.

$$M_{fuselage} = \frac{\sigma_t^{2/3} \sigma_c^{2/3} G S_f}{\rho c} \quad (3)$$

$$M_{fuselagframe} = \frac{E^{1/3} \sigma_y^{2/3}}{\rho c} \quad (4)$$

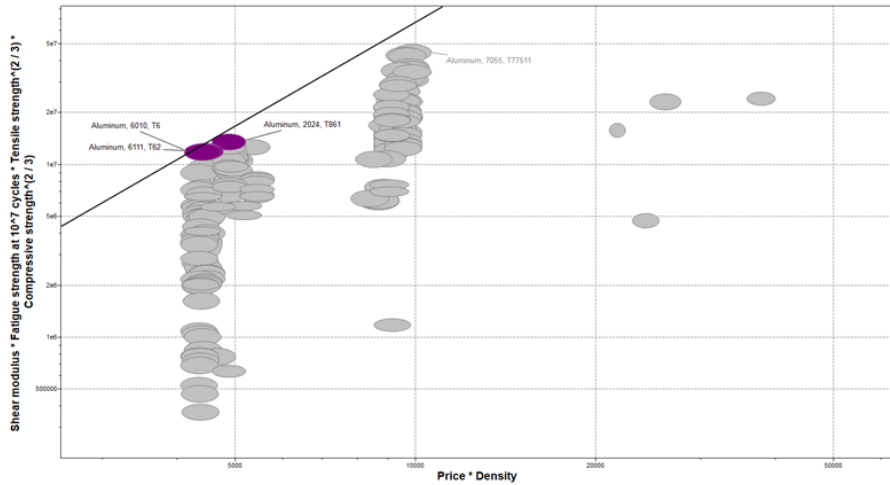


Figure 5: Ashby Chart for $M_{fuselage}$ with Design Guideline Slope of 1.5

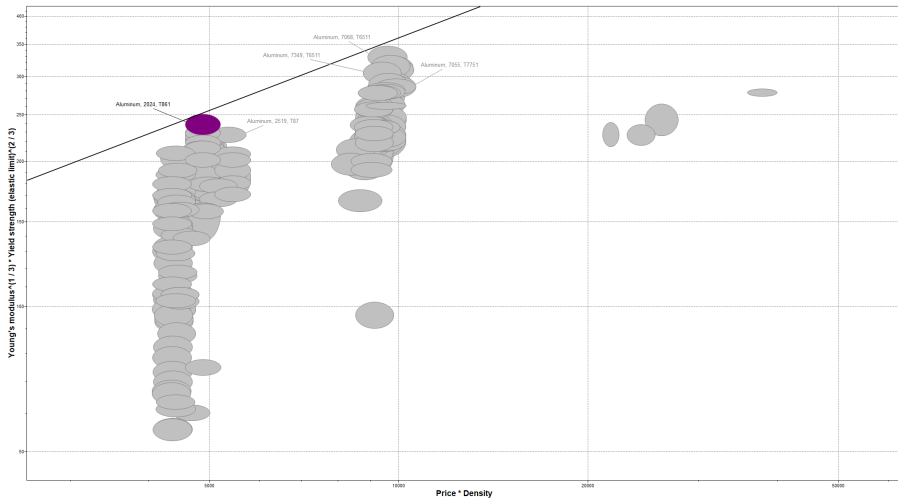


Figure 6: Ashby Chart for $M_{fuselagframe}$ with Design Guideline Slope of 0.5

With the aid of the Ashby charts shown in Figure 5, Aluminium 6111-T62 was the optimal choice for the fuselage skin. In Figure 6, Aluminium 2024-T861 was the best choice, however, during the optimisation

of the fuselage stringers, the compressive strength of the material was too constraining. The next best option was Aluminium 7068-T6511 however another 7 series aluminium alloy was selected for the upper wing skin. Although Aluminium 7055-T77511 was not an ideal choice, easier procurement of the two alloys instead of three and economies of scale should offset any mechanical property advantage Aluminium 7068-T6511 has.

3.3 Summary of Material Selection

The properties of the final materials chosen for the fuselage, wing and empennage are summarised in Table 3 . The values are obtained from the CES Material Selection Software [8] using mean values.

Table 3: Material Properties of the Aluminium Alloys Chosen

	Al 7055-T77511	Al 6111-T62
Density [kg/m ³]	2880	2695
Tensile Strength [MPa]	620	360
Compressive Strength [MPa]	610	320
Yield Strength [MPa]	585	320
Young's Modulus [GPa]	69	69
Shear Modulus [GPa]	25.6	27.6
Fracture Toughness [GPa]	29.7	33
Poisson Ratio	0.323	0.330
Price [£/kg]	3.44	1.65

4 Wing Design

The overall design flow of the wing box is shown in this section. The parts of a wing box could be separated into spars, skin stringer panels and ribs. Each of these would be discussed with assumptions, evaluations and verification.

4.1 Design strategy

The most efficient design of structure would be when all parts fail at the same point as the aircraft is a safety-critical system. However, it is hard to achieve as all parameters vary both spanwise and chordwise. Firstly, the worst-case scenarios during the flight and landing would be analysed, followed by the design and optimisation of spars and stringer panels. By integrating with the optimal rib design, the overall weight of the wing would match the target one calculated in the conceptual design. Other parameters would be used to evaluate the design's robustness and efficiency, such as the Farrar factor and the stress ratio.

4.2 Load Modelling

One large assumption made when modelling the aerodynamic loading of the wing was an elliptical load distribution [9] shown in Equation 5 where b_w is the span of the wing, y is the coordinate along the wing and $l_{wmax} = \frac{4nW}{\pi b_w}$ where n is the load factor and W is the weight of the aircraft; either MTOW or MZFW. The resulting lift distribution was given in Equation 6.

$$l_w(y) = l_{wmax} \sqrt{1 - \frac{y^2}{b_w/2}} \quad (5)$$

$$l_w(y) = \frac{4L_w}{\pi b_w} \sqrt{1 - \frac{y^2}{b_w/2}} \quad (6)$$

To model the wing inertial load, the assumption of a linearly varying weight distribution was used given below where λ_w was the taper ratio of the wing and W_{wmax} was the maximum point of the weight distribution at the root given in Equation 7 where w_w was the weight of the wing. Therefore the resulting

inertial load due to the weight of the aircraft was given in Equation 8.

$$W_{wmax} = \frac{2nw_w}{b_w(1 + \lambda_w)} \quad (7)$$

$$W_w(y) = \frac{2nW_w}{b_w(1 + \lambda_w)} \left(1 - \frac{1 - \lambda_w}{b_w/2} y \right) \quad (8)$$

The engine and the landing gear were assumed to be a point load placed at their respective centre of gravity and were augmented into $W_w(y)$. A similar procedure for finding the wing inertial load was used to find the load distribution of the fuel tanks and was put into $w_w(y)$.

The wing shear force (SF_w) and wing bending moment (BM_w) was trivial to find after finding the $l_w(y)$ and $w_w(y)$:

$$SF_w(y) = \int_y^{b_w/2} [l_w(y) - w_w(y)] dy \quad (9) \quad BM_w(y) = \int_y^{b_w/2} SF_w(y) dy \quad (10)$$

Each different load case has a varying effect on the overall wing torque. Contributions from the pitching moment, lift on the wing, the weight of the wing, thrust from the engine, fuel weight and payload(in this case engine weight) were taken into account to calculate the overall torque. Additionally, as this aircraft has a wing-mounted undercarriage, this was also taken into account in the final calculations. It is worth mentioning that all moments were calculated about the shear centre which when integrated along the whole semi-span of the wing is the flexural axis. This was taken to be mid-way between the front and rear spar as advised. To calculate the total torque distributed per spanwise coordinate of the wing, the torque from each of the components mentioned above had to be integrated from the edge of the fuselage to the wing tip, which can be seen in the following equation.

$$T(y) = \int_0^s [m_0 + t_{fuel} + t_{thrust} + t_{payload} + t_{aero} + t_{weight}] dy \quad (11)$$

The component of torque from the lift, t_{aero} was calculated using the sectional lift multiplied by the lifting moment arm, Equation (12). The lifting moment arm was taken to be the distance between the quarter chord point of the sectional aerofoil and the shear centre. The lift moment arm also incorporated the effect of both sweep and taper. The taper affected the distance between the aerodynamic centre and flexural axis by a constant ratio, and with the wing box cross-section taken parallel to the airflow it was easy to see that each section experiences additional torque due to sweep with the relation, additional torque is the product of the sine of flexural axis sweep angle and sectional bending moment. The camber from the chosen aerofoil for the wing is responsible for the zero lift pitching moment which has to be taken into account to calculate the torque. This was obtained using Equation (14), where C_{m0} is the coefficient zero lift pitching moment, V is either the manoeuvrable speed v_a or the dive speed V_{ne} (load case dependant), ρ is the density of the air, and c is the aerofoil sectional chord length. The pitching moment was then calculated for each section from root to tip. The proportion of total torque generated from the mass of the aerofoil was obtained by multiplying the moment arm from the shear centre of the sectional aerofoil with the centre of mass of each aerofoil section, with the weight of each section, given by Equation (13)

$$t_{aero} = L_{arm} W_{sec} \quad (12)$$

$$t_{weight} = L_{weight} * W_{secmass} \quad (13)$$

$$m_0 = \frac{1}{2} V^2 c^2 C_{m0} \rho \quad (14)$$

An additional torque generated from the engine thrust t_{thrust} and engine mass was also taken into account and modelled as a point load. The centre of mass of the fuel in the wing box was determined to act along the shear centre and hence its contribution was neglected. The total torque was then finally

determined for the wing and plotted, as seen in Figure (7c) for load cases 1 and 3 for Vne with MZFW (maximum zero fuel weight) which was found to be the most constraining case.

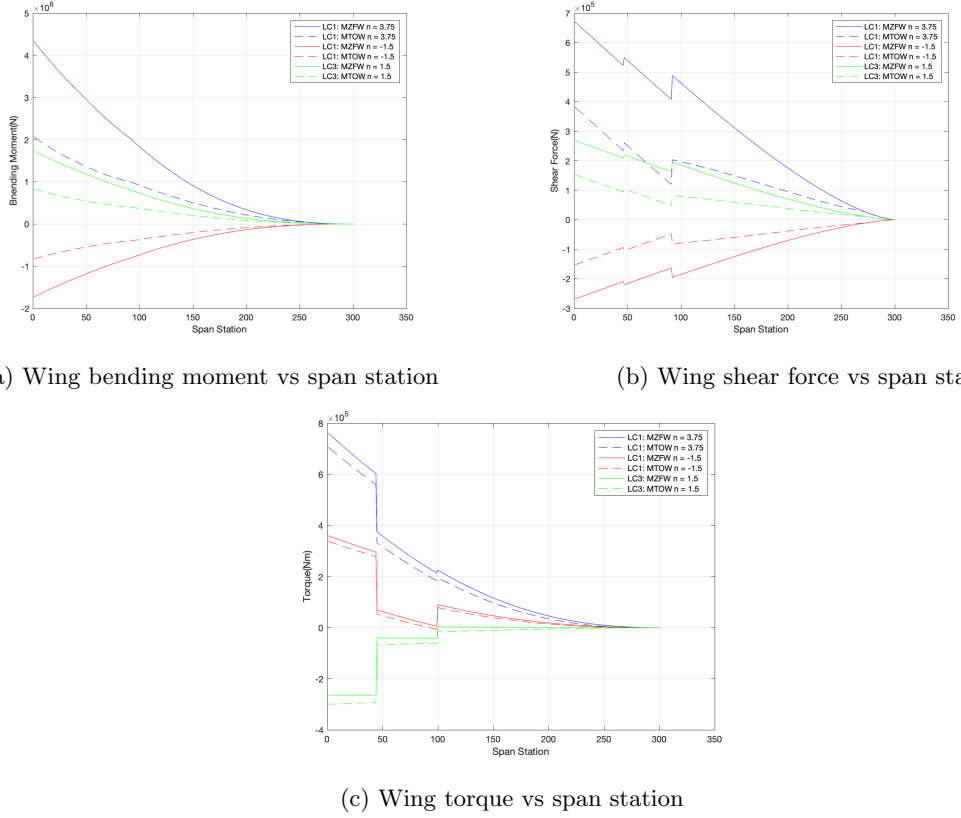


Figure 7: Graphs for load cases of wing

4.3 Spar Design

Spar is the component allocated along the spanwise which mainly undertaken the shear force, torque and bending moment. The first two are contributed by the aero loads and inertia loads in the chordwise direction and the bending moment comes along the span.

4.3.1 Geometry and Assumptions

In the conceptual design, it was stated that the wingbox contains two spars located at 10% and 75% of the local chord, hence the box width could be calculated as 65% of the chord length [5]. The web height could be calculated based on the aerofoil geometry from the Airfoil Tools. The aerofoil of the wing is NACA 64₁-212. At 10% and 75% of the chord, the y/c ratio is 4.577%, -3.448%, 3.462% and -1.669% respectively in terms of upper and lower skins [10]. By multiplying the local chord length, the web heights could be acquired. In terms of the method of calculating, it is assumed that the wingbox has a rectangular cross-sectional area. As a result, the most extreme load case would be applied to the web height of the rear spar and all the following calculations would be based on this. This may lead to overestimating the shear flow through the front spar but ensures the design of the rear spar would not fail at the design point. It is also assumed that the wingbox as an integrated component would take the bending moment together, therefore, the bending stress ratio would not be calculated in the spar design as it would not undertake all bending moments individually. Thus, the cross-sectional area of the spar is simplified to a rectangle where the height would be the web height. The flexural centre was assumed to be the middle of the wingbox. Another constraint to the spar design is that the main landing gear would be mounted at both front and rear spars which would not mitigate the anticlockwise torque generated by the aerodynamic loads. This would lead to a minor difference in the spar stress and thickness between the front and rear. Table 4 shows the box widths and the web heights at the root and the tip of the wing.

Table 4: Wingbox Geometry at the Root and the Tip of the Wing

Location	Box Width (m)	Front Spar Height (m)	Rear Spar Height / Web Height (m)
Root	3.74	0.451	0.285
Tip	0.897	0.101	0.0612

4.3.2 Sizing and Optimisation

As the assumptions mentioned, the shear flows contributed by shear force q_2 and torque q_0 could be calculated by using Equations 15 and 16, where T is the torque, A is the area of the cross-sectional area, b is the web height.

$$q_0 = \frac{T}{2A} \quad (15)$$

$$q_2 = \frac{SF}{2b} \quad (16)$$

Referring to Equation 17, the shear flows on the upper and lower skins would be zero and all of them would be distributed on the front and rear spars. By summing and subtracting the shear flows caused by shear force and torque, by using Equation 18, the thickness of spars could be calculated. V is the total shear flow of the spar and K_s is the shear buckling coefficient which would be optimised.

$$q = \frac{F_y}{I_x} \cdot D_x , \quad D_x = - \int_0^s y t ds \quad (17)$$

$$t = \sqrt[3]{\frac{V \cdot b}{K_s E}} \quad (18)$$

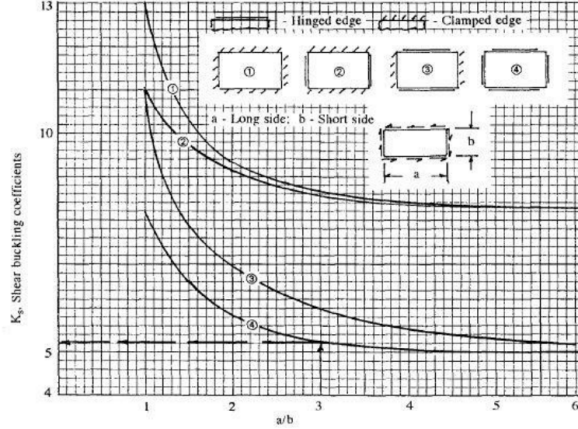


Figure 8: Shear Buckling Coefficient K_s Against the Aspect Ratio of a Plate under different Boundary Conditions [1]

Due to the reason that the tangential shear forces and torques would lead to a shear buckling, in the convenience of the first iteration, the shear buckling coefficient $K_s = 8.1$ was taken. This caused an overvaluation of the spar thickness and led to a mass that exceeded the budget. Figure 8 is a look-up figure which stated the relationship between the aspect ratio of plates and K_s . It contains four different boundary conditions while the all-clamped one was chosen as the spar would be firmly connected to the upper and lower skins. Table 5 shows the initial sizing of the spar shear flows, thicknesses and shear stresses at the root and the tip.

Table 5: Initial Sizing of the Spars at the Root and the Tip of the Wing

Location	Shear Stress (MPa)	Shear Flow (N/mm)	Thickness (mm)
Front Spar Root	228	2448	10.7
Front Spar Tip	1.55	0.636	0.410
Rear Spar Root	228	2448	10.7
Rear Spar Tip	1.55	0.636	0.410

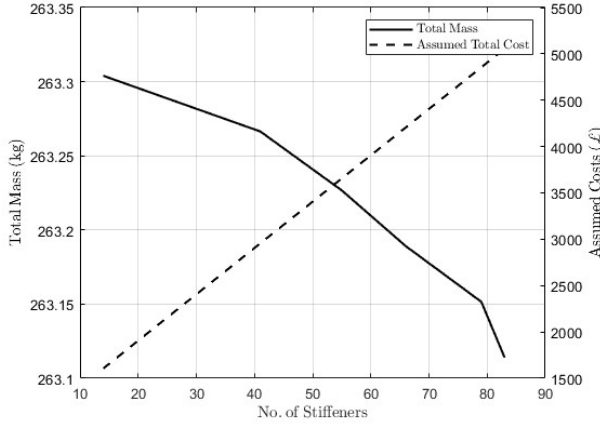


Figure 9: Total Mass and the Estimated Cost of the Spars Against the No. of Stiffeners

Since the initial sizing of the spar did not consider any stiffeners or flanges, the optimisation would be iterated based on this. With an increasing number of stiffeners, the aspect ratio of the plates along the spar would be decreased while the K_s would be increased. Figure 9 shows a trend of reducing mass when increasing the number of stiffeners. This would also lead to an increase in manufacturing costs. An estimation of the expense was made as it would cost £50 per stiffener attached. Figure 10 shows a comparison between the trend of spar mass against the root spar thickness. This figure was normalised based on the maximum mass respectively. A shear stress ratio was calculated.

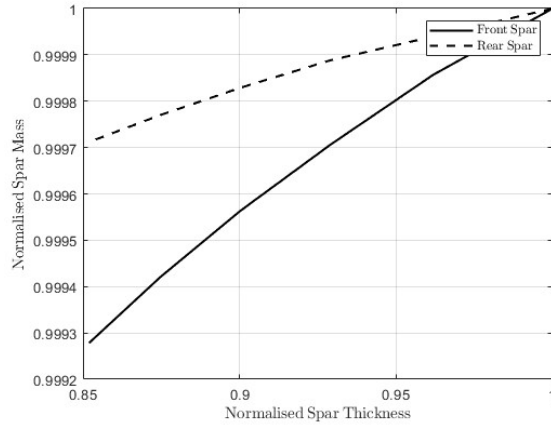
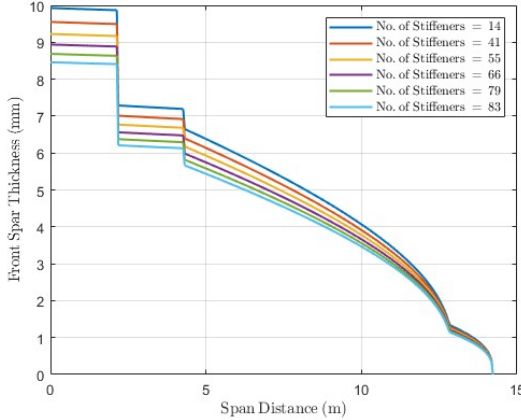
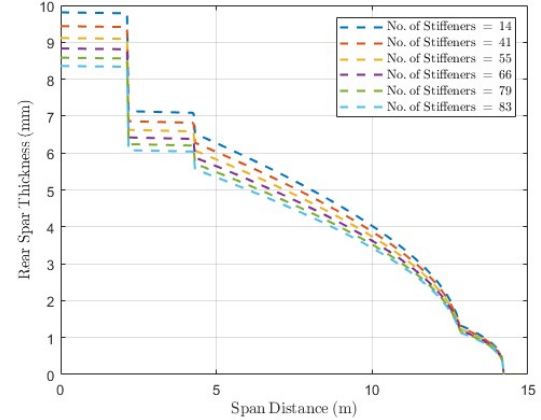


Figure 10: Normalised Spar Mass of Front and Rear Spars Against Normalised Root Spar Thickness

Figures 11a and 11b show the spanwise distribution of the spar thicknesses of both front and rear spars with different numbers of stiffeners attached. Due to the limitation of manufacturing and clearances, the lower limit of the thickness would be 1 mm. Figures 12a and 12b show the modification of spar thickness across the span in consideration of the manufacturing.

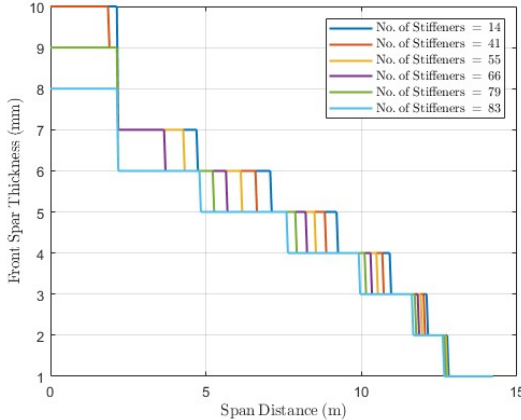


(a) Front Spar Thickness Variation

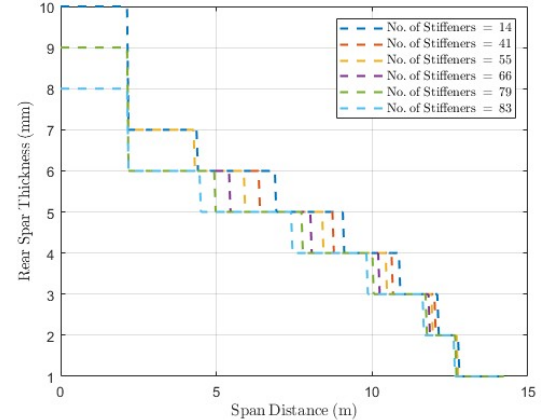


(b) Rear Spar Thickness Variation

Figure 11: Front and Rear Spar Thickness Distribution Along the Span



(a) Front Spar Thickness Variation



(b) Rear Spar Thickness Variation

Figure 12: Spanwise Thickness Distribution with Manufacture Concerned

4.4 Skin Stringer Panels Design

The integration of skins and stringers is essential for the reduction of mass and increase of structural efficiency while taking the same amount of stress [11]. A comparison between the unflanged skins and skin stringer panels would be made.

4.4.1 Geometry and Assumptions

The bending moment would lead to compressive and tensile loads to the upper and lower skins respectively. It is assumed that these loads would be equivalent in magnitude and evenly distributed. This simplifies the design process but brings the overestimation of the lower skin stringer thickness. It is assumed that the overall bending moment would be solely taken by the skin stringer panels, which is also an overvaluation of the thickness. As mentioned in the Spar Design section, the same wingbox width and web height would be used. A Z-section would be the shape of the stringers for high structural efficiency [3].

4.4.2 Sizing and Optimisation

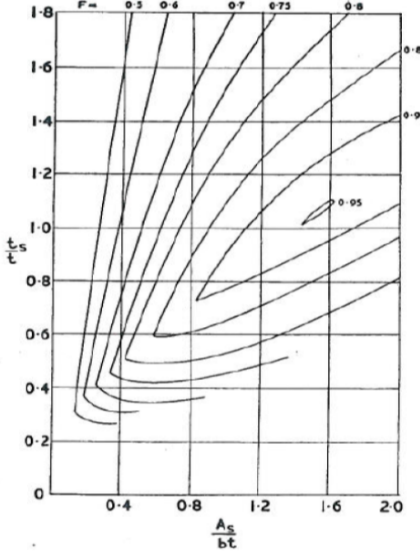


Figure 13: Farrar's Efficiency Factor (F) for Z-Stringer Panels [2]

The number of independent variables was one of the obstacles in the overall design process. For reducing the dimensions of the designing matrices from 4-D to lower degrees, several assumptions were made. Figure 13 shows the relationship between t_s/t , A_s/bt and the Farrar factor, where t_s is the stringer thickness, t is the skin thickness, A_s is the cross-sectional area of the stringers and b is the panel width in between two consecutive stringers. In theory, the most optimal Farrar factor F would be $F > 0.95$ with the assumption of the flexural-torsional coupling is small [3]. This would be unachievable in reality as the variation of both stringers' and skins' thickness. Therefore, an $F > 0.7$ would be considered an acceptable design [2]. To achieve this, several groups of t_s/t and A_s/bt were tested while F satisfies the minimum requirement. For further simplification, two other constants were set. $h/b = 0.8$ and $d/h = 0.3$ where h is the web height. Figure 14 shows the trend of the buckling coefficient varying with the t_s/t . Refers to Equation 19, where N is the compressive load, the stringer and skin thicknesses (t_s and t_2) could be calculated, so as the critical buckling stress and critical shear stress by Equation 20.

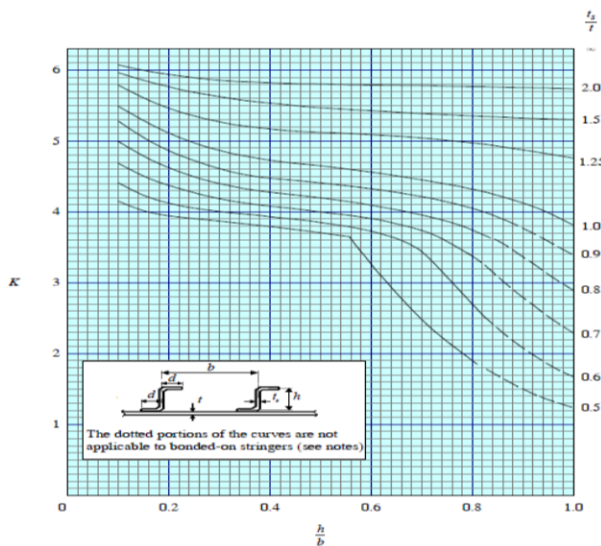


Figure 14: K and $\frac{t_s}{t}$ Against $\frac{h}{b}$ for Z-Stringer Panels [3]

$$\frac{N}{t_2} = 3.62E \left(\frac{t_2}{b} \right)^2 \quad (19)$$

$$\tau_0 = \frac{N}{t_2} \quad (20)$$

By comparing the combination of ratios from the look-up figures, the optimum values which satisfy the selection criteria with results that minimising the mass would be $\frac{t_s}{t_2} = 0.4$, $\frac{A_s}{bt} = 0.64$ and $K = 1.8$. At this point, further design decisions would be based on these ratios.

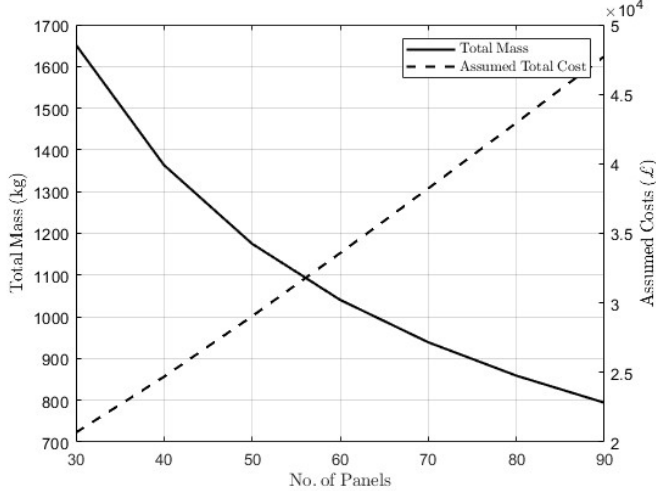


Figure 15: Total Mass of Stringer Panels of two Wings Varies with the No. of Panels

As a result, the only independent variables left would be the number of panels and the rib spacing and the optimisation iterations would be based on these. Figure 15 shows that the increasing number of panels reduces the mass but leads to an increase in manufacturing.

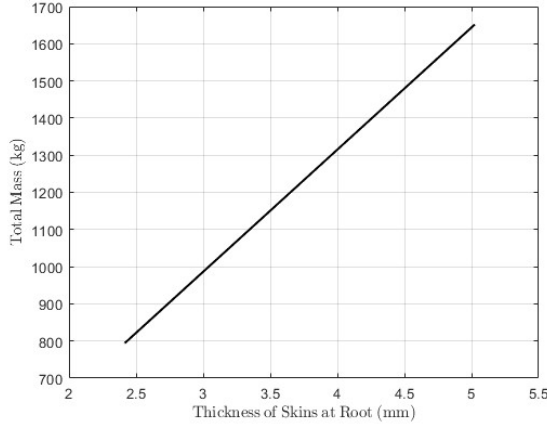


Figure 16: Total Mass Against Root Skin Thickness

Figure 16 shows the root skin thickness variation along with the changes in the total mass of the wing, with different numbers of panels. The correct trend proves the reliability of the optimisation. Figure 17a and 17b show the changes in stringer thickness and height along the span. It was noticed that due to the limitation of clearance, cost and manufacturing, a minor change of less than 0.1 mm would not be achieved. Figure 18 shows the stringer thickness in the spanwise direction after being modified by manufacturing limits.

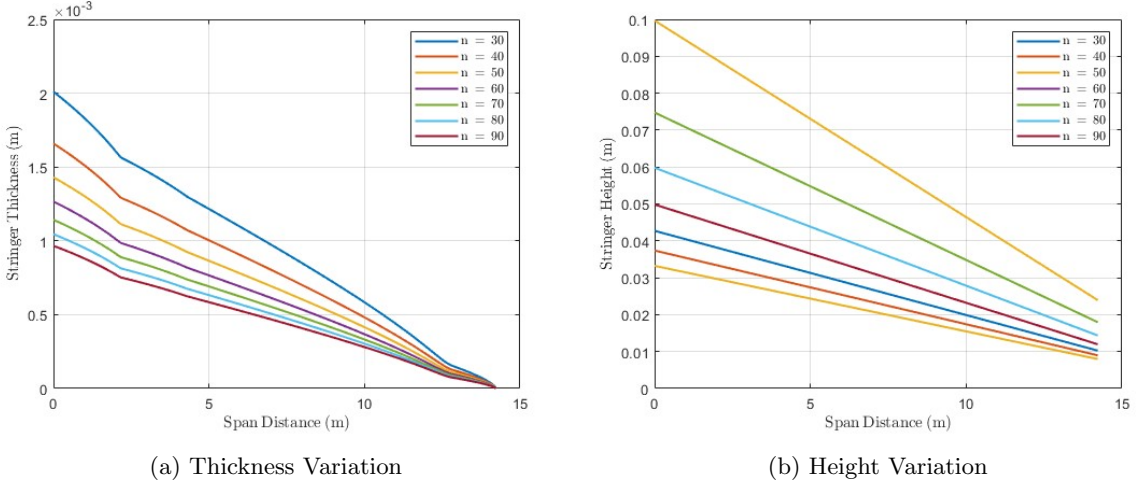


Figure 17: Thickness and Height Distribution Along the Span

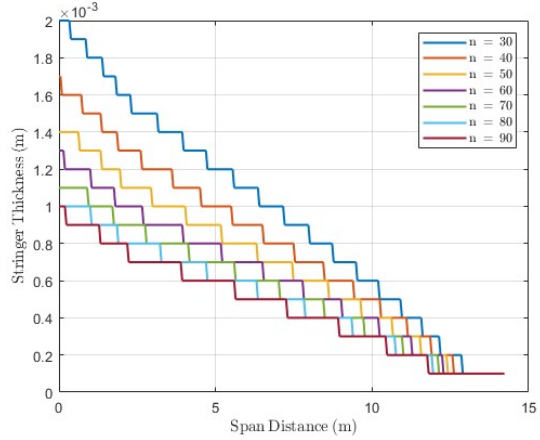


Figure 18: Modification with Clearance and Tolerance Concerns

As the Farrar factor would be used for ensuring the validity of the design, Figure 19 shows the changes in F spanwise with different numbers of panels. It could be seen that the circumstances fall at the tip but correspondingly the tip would be less structurally considered but more considered of the aerodynamic performances.

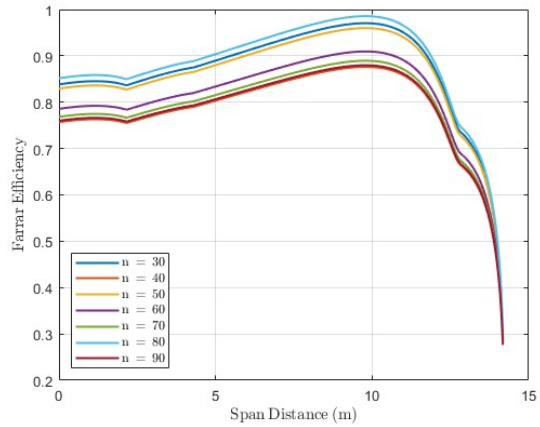


Figure 19: Farrar Factor Distribution Along the Span

4.5 Rib Design

The weight optimisation was done based on finding out the optimum rib spacing, L, required, with which each individual rib can survive the wing crush loads experienced by the wing due to its curvature.

The crush load F_{crush} is calculated for each span station division, given by Equation 21, where BM is the bending moment, L is the rib spacing, h_c and c_r are the height and width of the rib respectively, t_{eff} is the effective thickness of the skin stringer panel, I is the second moment of inertia and E is the Young Modulus.

$$F_{crush} = \frac{BM^2 h_c c_r L T_{eff}}{2I^2 E}. \quad (21)$$

$$t_{eff} = t + \frac{t_s h}{b} \quad (22)$$

$$I = t_{eff} c_{b_{wing}} \left(\frac{b_{b_{wing}}}{2} \right)^2 + (\rho_{wing})^{2t_{eff}} c_{b_{wing}} \quad (23)$$

then the critical buckling load for each span station division, σ_{cr} can be equated to the actual stress σ_r in each section and can be rearranged for rib thickness, t_r , giving the required minimum skin thickness in each section.

$$\sigma_{cr} = 3.62E \left(\frac{t}{h} \right)^2 \quad (24)$$

$$\sigma_r = \frac{F_{crush}}{t_r C} \quad (25)$$

$$t_r = \left(\frac{F_{crush}}{3.62Ec} \right)^{1/3} \quad (26)$$

Now that the minimum rib thickness for each section was found, a graph of the total weight was plotted of the stringers and rib mass was plotted, as can be seen in Figure 20. Using this graph, it was determined that the value of L is 0.4 m, which is in line with that of typical aircraft of this configuration, further validating the calculation. It is worth noting that the total mass with the chosen rib spacing lies well within the design weight for the wing.

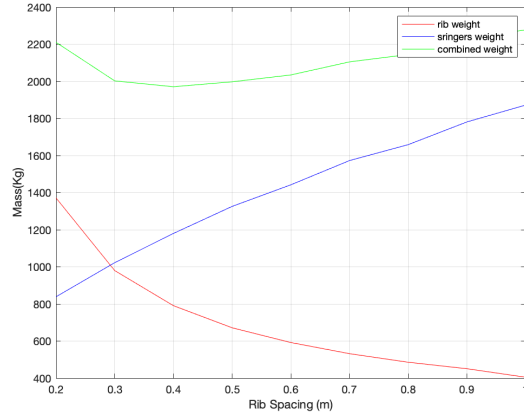


Figure 20: Stringer and Rib Weights VS. Rib Spacing

4.6 Geometry & Mass Summary

4.6.1 Geometry

Table 6: Wing Rib Geometry sample Summary with Rib Spacing of 0.4 m

Rib Dimensions	1	5	10	25	39
Rib Thickness [mm]	1.0619	0.9353	0.7756	0.2512	0.0595

Table 7: Wing Spar Web Geometry at the Root

Spar Web	
Front Spar Thickness [mm]	9.225
Rear Spar Thickness [mm]	9.115
Number of Stiffeners	55

4.6.2 Mass

The mass budget left for the wing section in the conceptual design would be 3326.868 kg [5]. With the combined mass of spars, stringer panels and ribs, the target structure mass would be aiming at 2500 kg with the rest left for the deployable mechanism, control surfaces and other components. As mentioned in the Rib Design, the combined mass of stringer panels and ribs would be around 1970 kg and from the Spar section the mass would be about 263.3 kg. Table 8 shows the optimally designed mass of each component, the optimal number of panels, stiffeners and rib spacing. Although the design point of the panels' amount is less than that of the optimum, the estimation of pricing may vary and the total mass budget of the wings is met according to this design.

Table 8: Mass Breakdown for the Wing Components

Component	Skin	Spar	Rib	Total	Estimated Total
Weight [kg]	1175	263	790	2229	2500

4.6.3 Stress Ratio

As the skin would mainly undertake the shear forces and compressive/tensile loads from the bending moment, refers to the Equation 27, the stress ratio of the skin stringer panels shall be kept below 1. Figure 21 shows the spanwise variation of the ratios and all of them would be less than 1 which implies that this design is with high efficiency.

$$R_s^2 + R_c \leq 1 \quad (27)$$

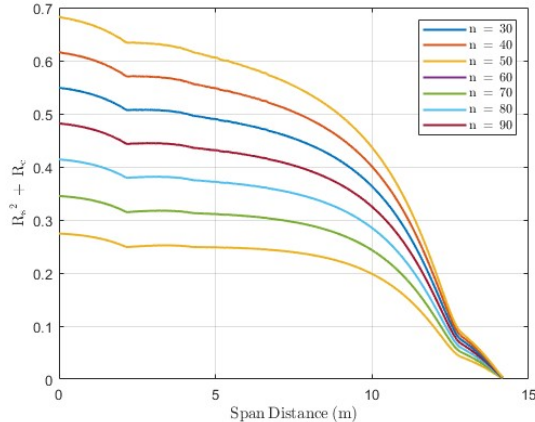


Figure 21: Stress Ratio Along the Span

5 Fuselage Design

The primary function of the aircraft fuselage is to house passengers, crew, and payloads. Therefore, the fuselage airframe is designed to provide the passages and crews with a comfortable experience of travelling in high altitudes at a suitable pressurisation level and protect the internal components from various loading situations. In this design project, three loading cases - symmetrical flight at ultimate load factor, OEI, and nose-off landing - are considered to size the skin, stringers, and frames of the fuselage to achieve a minimum weight design.

5.1 Design Strategy

Idealising the fuselage as a beam to apply the Engineer's Theory of Bending [3] to simplify the design process, the maximum loading scenarios are first calculated from the three loading cases to obtain the most extreme shear force, bending moment, and torque. The key aim of the sizing is to achieve the minimal possible weight that resists the worst-case scenario. The skin is sized according to pressurisation, shear, and torque, whereas the stringers are designed to withstand the longitudinal stress due to the bending moments. Frames are designed to prevent stress concentration, general stability, and failure. As the sizing of these airframe components is heavily coupled, the stringer thickness was chosen to vary between 1.6 to 4 mm, based on the historical data obtained from Airbus[4]. Geometric constraints are also enforced under the assumptions of the following ranges, summarised in Table 9 to avoid discontinuity in super-stiffener geometry in the iterating process in optimisations.

Table 9: Fuselage Stringer-skin Design Variable Range[4]

	Lower Bound (mm)	Upper Bound (mm)
Stringer Height (h)	25.0	55.0
Stringer Width (d)	8.00	26.0
Skin Thickness (t)	1.60	8.00

Finally, buckling analysis of the chosen components was conducted to prevent general instability and ensure the structural integrity of the fuselage.

5.2 Load Cases

5.2.1 Mass Distribution

The fuselage was discretised to 3180 stations with a constant mesh size of 0.01m along the nose in the x direction to obtain the load, shear, and bending for each loading case. Although this spacing is much smaller than the typical frame spacing, a finer mesh ensures more accurate results in calculating these values. Each station is assigned to carry a distributed mass. In the section of Weight and Balance in Conceptual Design [5], the mass of aircraft key components and their CG were found, suggesting the mass can be assigned to the corresponding station as a point load. However, to consider the effect of wiring, Poisson Distribution was used for distributing mass for components, such as instruments, by setting the expected value to be its corresponding CG, while for components like furnishings, assigning mass to each station with range by a constant distribution was more reasonable. Detailed mass distribution is shown in the Table 10, and the mass distribution result at each station with a distance of x with respect to the nose is shown in Figure 22. Due to the nature that Poisson Distribution was originally only applicable for random variables, and for components with smaller range, the mass can not be fully distributed to the stations. Hence, results from this method lost 157 kg of mass in total.

Table 10: Mass Distribution Type for Each Aircraft Component

Component	Mass (kg)	x-positions (m)	Lower Bound (m)	Upper Bound (m)	Type
Handling Gear	13.77	0.00	0.00	0.00	Point
Avionics	971.31	1.14	0.00	5.50	Contant
nlg	302.37	3.10	0.92	3.30	Poisson
Instruments	108.93	3.00	0.00	5.50	Poisson
Fuel	5390.00	9.74	8.09	11.39	Poisson
Fuel syst.	213.87	10.76	8.00	14.15	Possion
Elec. syst	326.34	10.76	0.00	25.02	Constant
Hydraulic syst.	85.88	11.96	2.51	26.80	Constant
Furnishings	2449.15	12.72	1.50	25.02	Constant
Fuselage	5147.79	13.74	0.00	31.80	Constant
Total Payload	9285.00	14.15	1.50	22.90	Constant
flight cont.	501.12	15.67	1.50	26.80	Constant
Air-Con	512.23	15.90	1.50	25.02	Constant
VT	346.65	24.12	22.75	26.80	Possion
HT	407.75	26.80	25.81	29.74	Possion
APU	149.69	30.21	29.18	31.35	Possion

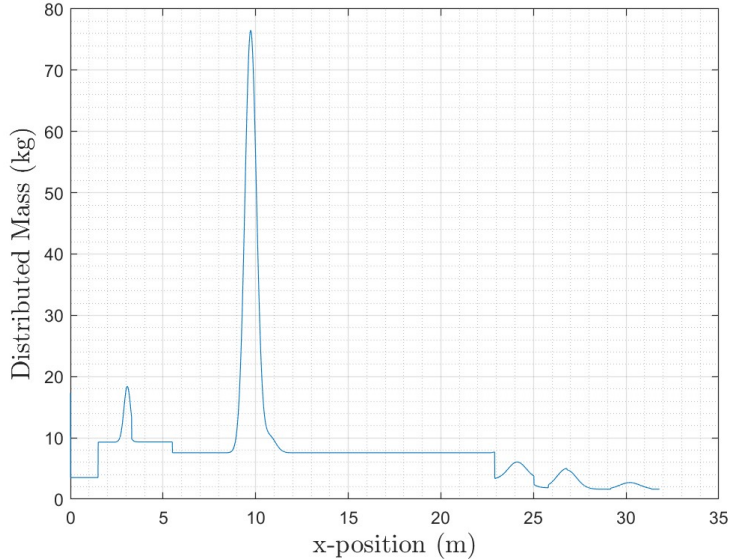


Figure 22: Distributed Mass vs x-Positions from the Aircraft Nose

5.2.2 Load Case 1: Symmetric Loading at Ultimate Load Factor

The loading of symmetric flight at the ultimate load factor can be determined as a combined effect of inertial and aero load. In this design, the ultimate factor $n = 2.5$ [3] was used, and all calculations include a safety factor of 1.5. At cruising conditions, the reaction force on the front and rear spars can be found by solving a statically determinate beam problem with Force and Moment Equilibrium.

$$R_F + R_R = \sum_{i=1}^N w(x_i) \quad (28)$$

$$R_F L_F + R_R L_R = \sum_{i=1}^N x_i w(x_i)$$

where (R_F, L_F) and (R_R, L_R) are the front and rear spar reaction forces and their respective distances relative to the origin at the nose, respectively. N is the number of stations. Solving the equation

gives $R_F = 3.912 \times 10^5$ N and $R_R = -6.04 \times 10^5$ N. To maintain an equilibrium flight, a tail load of $R_T = 2.13 \times 10^5$ N is required to apply at the horizontal stabiliser in the x -direction.

As the fuselage is idealised as a beam, Engineer's Bending Theory can be applied to calculate the resulting shear force and bending moment by simply integrating the weight at the station once and twice respectively.

$$S(x_j) = - \sum_{i=1}^j w(x_i) \quad (29)$$

and

$$M(x_j) = - \sum_{i=1}^j \sum_{i=1}^j w(x_i) \quad (30)$$

where $1 \leq j \leq N$ is the index of the station of which the shear and bending are examined. It can be noted that the shear and bending moments at the nose and the fuselage end are zero.

The results are shown in Figure 23.

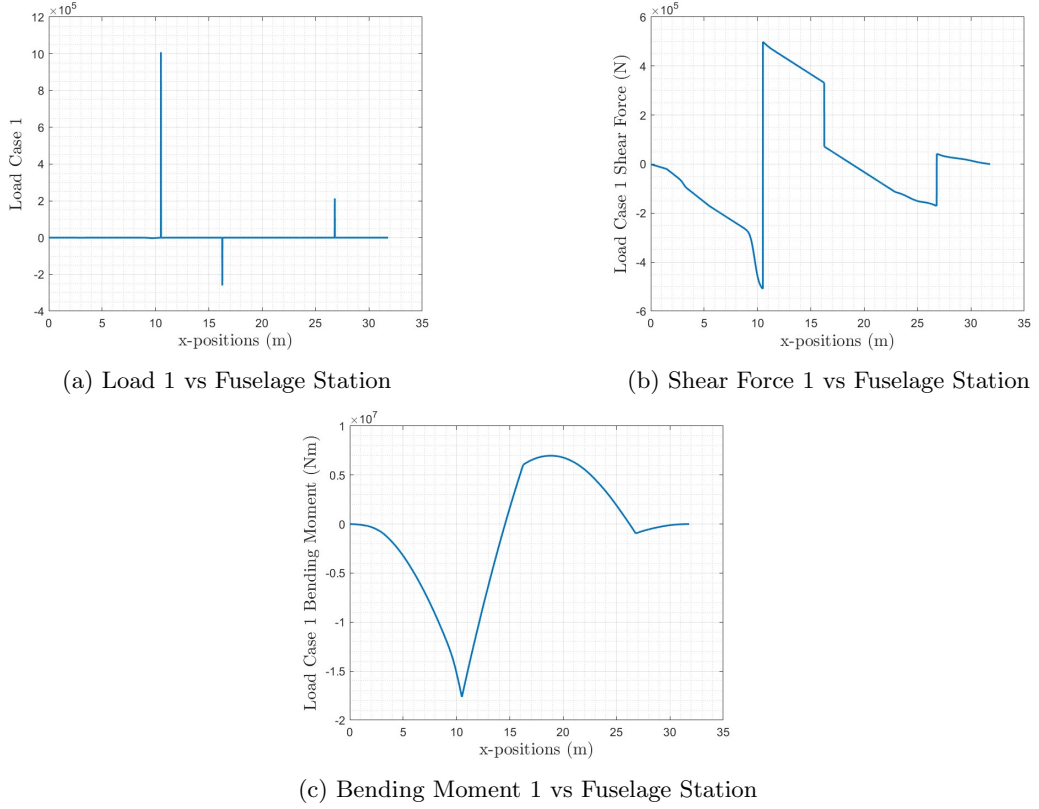


Figure 23: Load Case 1 Results

5.2.3 Load Case 2: Asymmetric Loading at OEI

For Asymmetric OEI loading, the assumption of zero-degree side slip angle is assumed. This assumption gives rise to two moment equilibrium equations about the aircraft nose and CG as shown in Figure 24. The distributed reaction force R_{FVT} and R_{RVT} on the front and rear spars of the vertical stabiliser can be calculated respectively using the total resultant R_{VT} on the vertical tailplane obtained from the OEI loading section by

$$R_{FVT} + R_{RVT} = R_{VT} \quad R_{FVT}(L_{xFVT} - x_{VT(cg)}) + R_{RVT}(L_{xRVT} - x_{VT(cg)}) = 0 \quad (31)$$

where L_{xFVT} denotes the distance of front vertical stabiliser spar in the x-direction, and $x_{VVT(cg)}$ is its CG with respect to the aircraft nose. As chosen in the conceptual design stage [5], the front and rear spars of the vertical stabiliser are at 15% and 65% of the chord, and hence their distance to the aircraft nose and CG can be subsequently calculated.

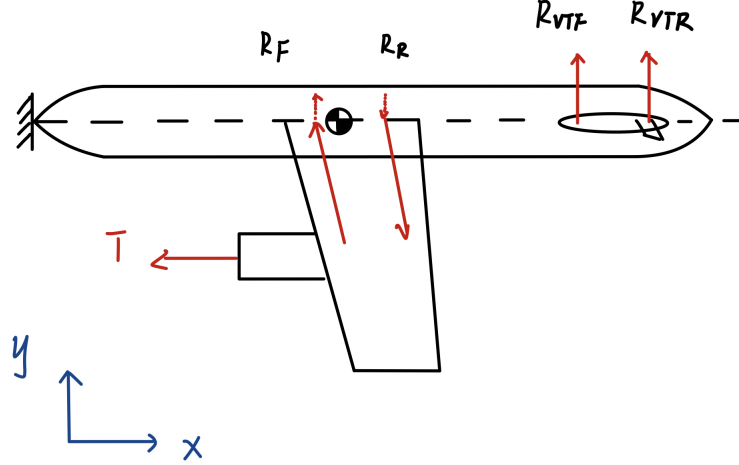


Figure 24: Load Case 2 OEI Moment Equilibrium (Drawn not to Scale)

The loads on the front and rear spars of the wing can then be found by

$$R_F L_{xF} + R_R L_{xR} = -T(L_{yE} - y_{CG}) - R_{FVT} L_{xFVT} - R_{RVT} L_{xRVT} \quad (32)$$

for moment equilibrium about the aircraft nose, and

$$R_F(L_{xF} - x_{CG}) + R_R(L_{xR} - x_{CG}) = -T(L_{yE} - y_{CG}) - R_{FVT}(L_{xFVT} - x_{CG}) - R_{RVT}(L_{xRVT} - x_{CG}) \quad (33)$$

for moment equilibrium about the aircraft CG. L_{yE} denotes the distance of the engine to the aircraft CG in the y-direction. The thrust $T = 71.2$ kN is obtained from P&W PW815GA engines chosen in the conceptual design stage [5]. Shear force and bending moment, shown in Figure 24 can be calculated in a similar way as in Loading Case 1.

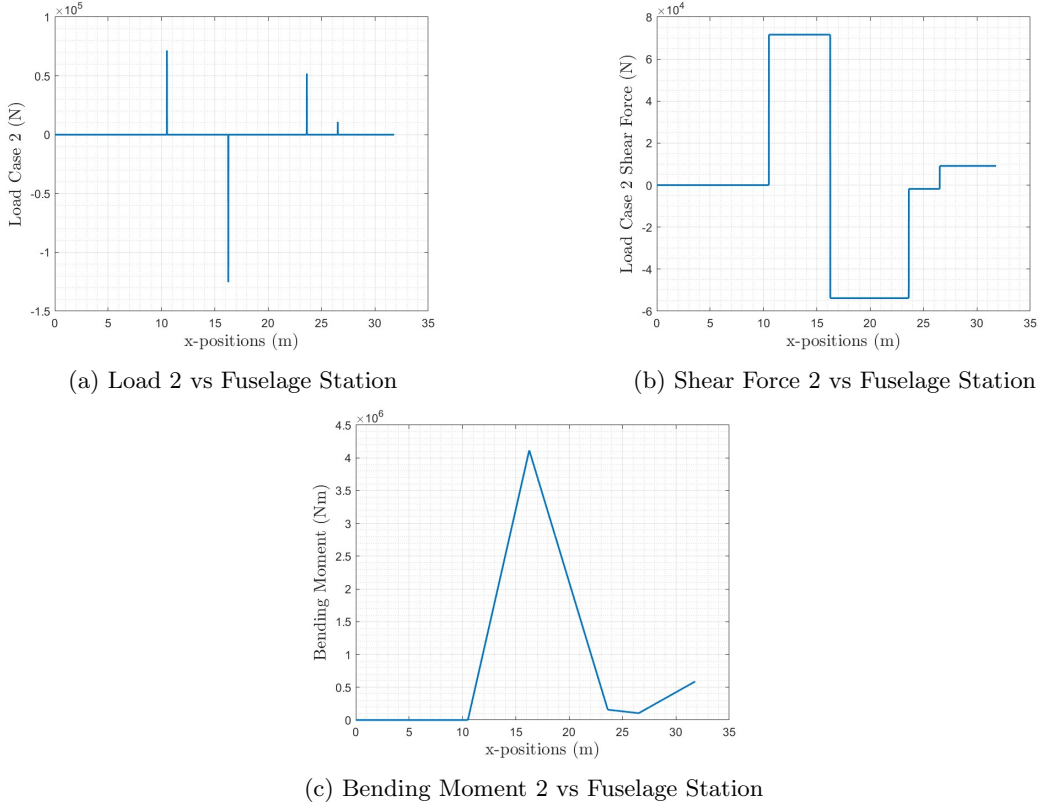


Figure 25: Load Case 2 Results

5.2.4 Load Case 3: Loading at Nose-off Landing

In this loading case, the main landing gears take up the majority of the loading. A gear load factor of $n = 3$ for General Aviation [3] is considered and multiplied by a safety factor of 1.5. Shear and bending are found through ETB, the same way as calculated in Load Case 1.

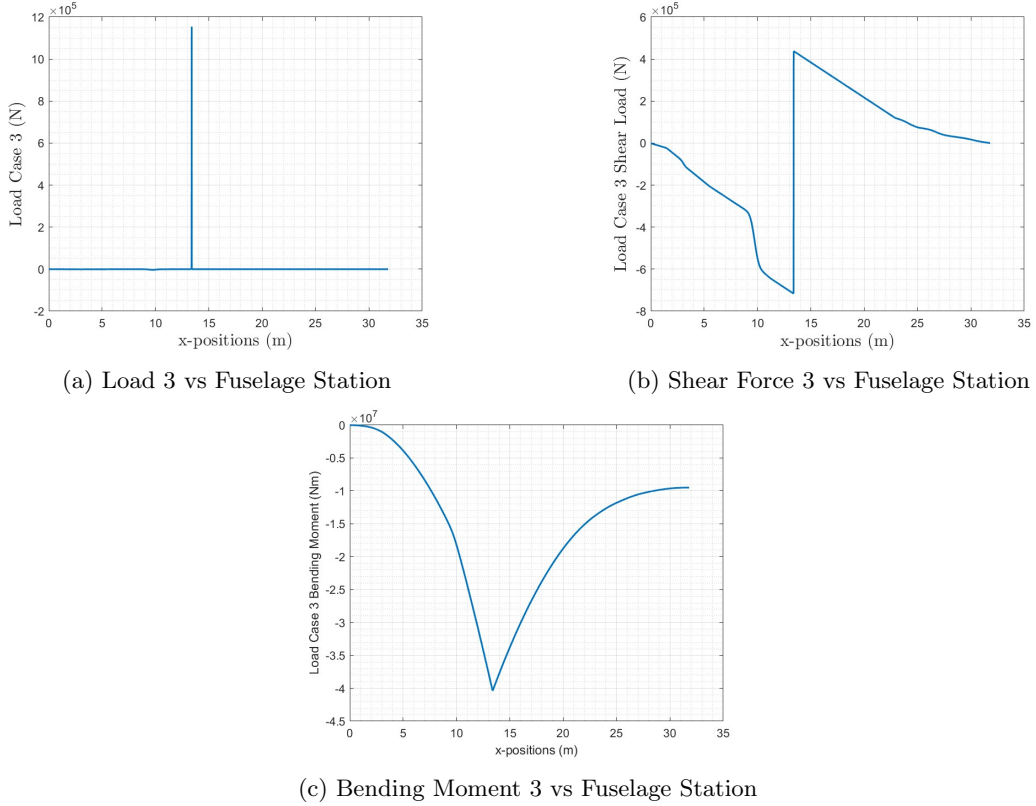


Figure 26: Load Case 3 Results

5.2.5 Maximum Loadings Summary

The maximum shear force, bending moment, and torque, if applicable, among the three loading cases are summarised as follows. These values are the most constraining cases to size the fuselage in terms of skin, stringer, and frame.

Table 11: Maximum Shear Force, Bending Moment, and Torque of Fuselage Loading Cases

	Shear Force (N)	Bending Moment (Nm)	Torque (Nm)
Load Case	1	3	2
Maximum Value	2.45E+06	4.04E+07	4.10E+07

5.3 Pressure Loads

In order to design for the pressure loads experienced by the aeroplane at an absolute ceiling of 40,000 ft [12], it was modelled as a cylinder of radius 3.5 m with two hemispherical caps at either end. The fuselage was taken to be pressurised at the typical pressure of 0.7 BAR [2] and the atmospheric pressure at 40,000 ft was found to be 0.188 BAR [13], thus giving a pressure difference of 0.512 BAR.

It is highly desirable to minimise the bending in the structure and so the thickness of the cylindrical and hemispherical sections was designed such that the strains across them were the same. To do this, equations 34 and 35, where t_1 and t_2 are the thicknesses of the cylinder and hemisphere respectively, were equated.

$$\varepsilon_H = \frac{1}{E}(\sigma_H - \nu\sigma_L) = \frac{pd}{4Et_1}(2 - \nu) \quad (34)$$

$$\varepsilon_H = \frac{1}{E}(\sigma_H - \nu\sigma_H) = \frac{pd}{4Et_2}(2 - \nu) \quad (35)$$

This resulted in a thickness ratio of

$$\frac{t_1}{t_2} = \frac{2 - \nu}{1 - \nu} \quad (36)$$

and thus once a value for the cylindrical thickness was found, the hemispherical thickness could be sized accordingly.

Using the yield stress of the material as the maximum value of hoop stress, equation 37 was used to calculate t_1

$$\frac{\sigma_H}{P} = \frac{d}{2t_1} \quad (37)$$

and so the skin thicknesses required due to pressurisation can be seen in the table below.

Table 12: Key Values and Dimensions for Pressure Sizing

Pressure Load (bar)	t_1 (mm)	t_2 (mm)
0.512	0.280	0.112

5.4 Stringer-Skin Design

5.4.1 Skin

In order to design the stringers and skin, the stringers were idealised as equally spaced discrete elements, or booms, which only carry direct stress, while the panels between them carry the shear force. The boom area comprised of the skin equivalent area, which was taken to be 15 times the skin thickness, and the stringer area. The final choice of stringer shape was a machined Z-stringer: while integrated would result in a lower mass, manufacturing costs would be significantly higher and the process more complex. A hat shaped stringer was also considered; however, when taking into account the likely high number of stringers, it was decided that the risk of corrosion if water were to get into the enclosed space was too high. In addition, it would be very time consuming and tedious to have to check every one.

In order to size the skin, the shear flow was calculated around the skin using equation 38 and the maximum value from this used to give a minimum thickness to resist this shear.

$$q = \left[\frac{T + Pr}{2\pi r^2} + \frac{P\cos(\phi - \alpha)}{\pi r} + \frac{Q\sin(\phi - \alpha)}{\pi r} \right] \quad (38)$$

Q , P , and T refer to the radial load, tangential load and the torque respectively. The skin thickness was calculated for two load cases which were determined to be the most constraining: load cases 1 and 2, the values for which can be seen summarised in the table below:

Table 13: Summary of Q, P and T Values for Load Case 1 and 2

	Q (MN)	P (MNm)	T(MNm)	q_{max} (MN/m)	t (mm)
Load Case 1	2.45	0.00	0.00	0.445	2.78
Load Case 2	0.548	0.00	0.303	0.0263	0.160

As can be seen, the maximum shear that needed to be designed for was that of Load Case 1. The shear flow distribution can be seen in Figure 27. The final value for skin thickness was taken as the summation of the required thickness for pressure load, 0.28 mm, and shear, 2.78 mm, giving a final value of 3.06 mm.

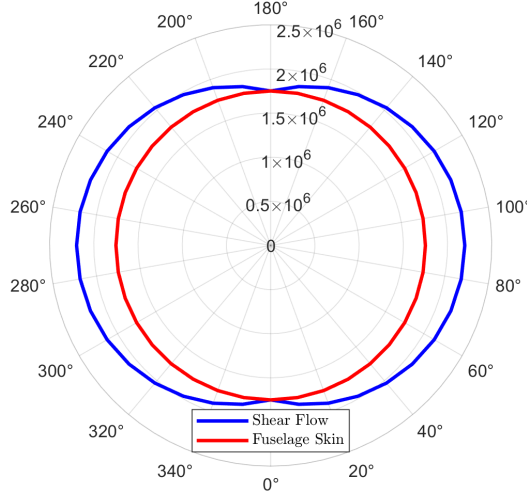


Figure 27: Shear Flow Around Fuselage Skin

5.4.2 Stringers

The next step was to design the stringers themselves. These were required to withstand the maximum bending moment that the fuselage would undergo, found to be 4.04×10^7 Nm. For each n number of stringers, the minimum area was found iteratively by trialing increasing increments of area values until the maximum stress within the stringers was less than that of the yield stress of the material. To determine the corresponding dimensions for each area, an initial ratio of

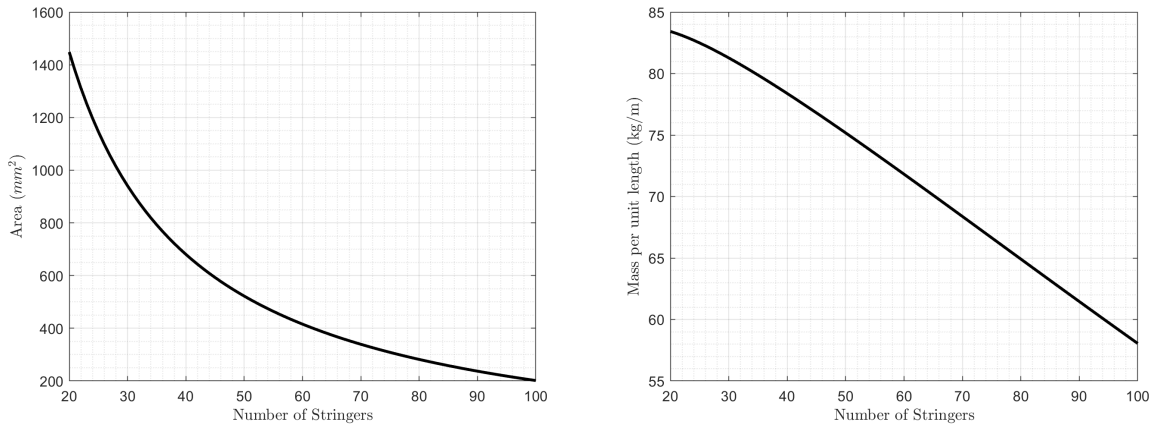
$$\frac{A_s}{bt} = 0.3 \quad (39)$$

was trialed, where A_s is the stringer area; however this did not allow us to achieve the recommended dimensions as will be later discussed. Thus a final ratio of

$$\frac{A_s}{bt} = 0.5 \quad (40)$$

was chosen. As is conventionally chosen, the ratio of width to height of the stringer was decided to be 0.3 [14] and from these two conditions, all dimensions of the stringer could be calculated.

A graph of stringer number against area was plotted, as seen in Figure 28a, to visually see the relationship, and it was found that as the number of stringers increased, the mass per unit length of the fuselage in fact decreased, displayed in Figure 28b.

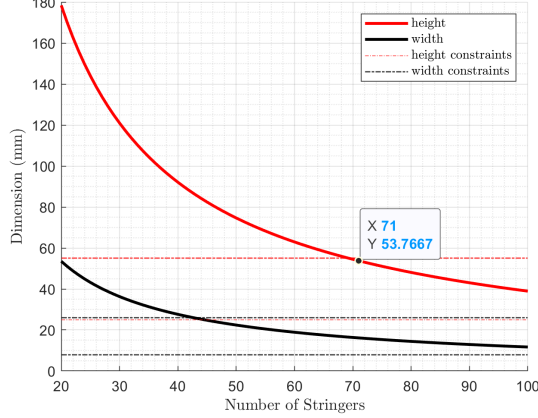


(a) Stringer Area VS. Stringer Number

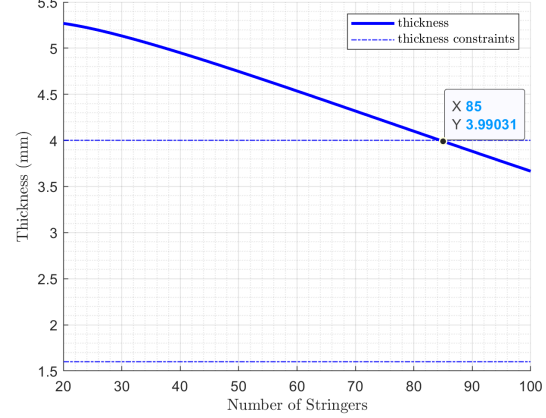
(b) Mass per Unit Length VS. Stringer Number

Figure 28: Relationships between area, mass and stringer number

As weight was not a constraint in this case, a maximum bound of 87 was set based on similar aircraft and also with the aim of not having too small a pitch between stringers. The minimum number of stringers was decided based off dimension guidelines given in [7]. These guides can be seen plotted in figures 29a and 29b and thus the minimum number of stringers such that our stringers were of a recommended dimension was 85 due to the most constraining case of having a small enough thickness.

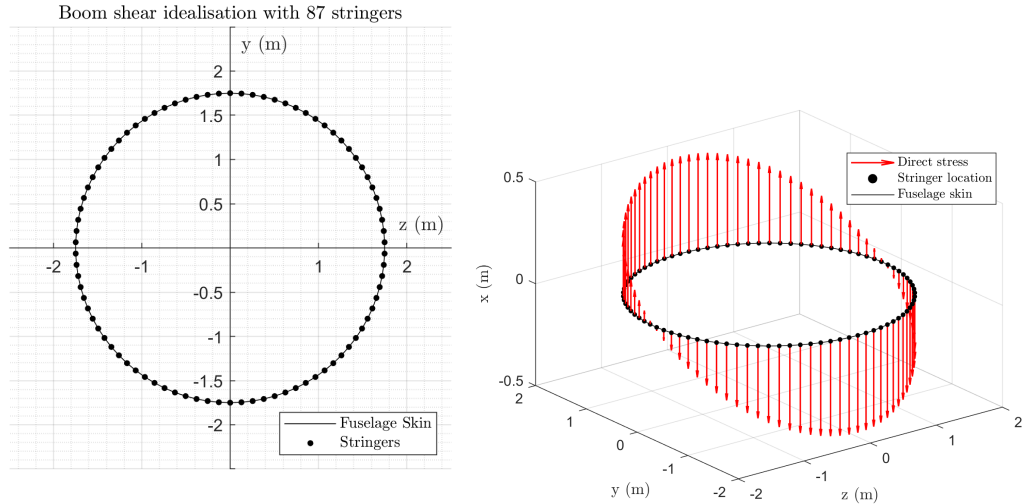


(a) Width Constraints to a Minimum of 71 Stringers.



(b) Thickness Constraint on Stringer Number

Figure 29: Dimensional Constraints on Stringer Number



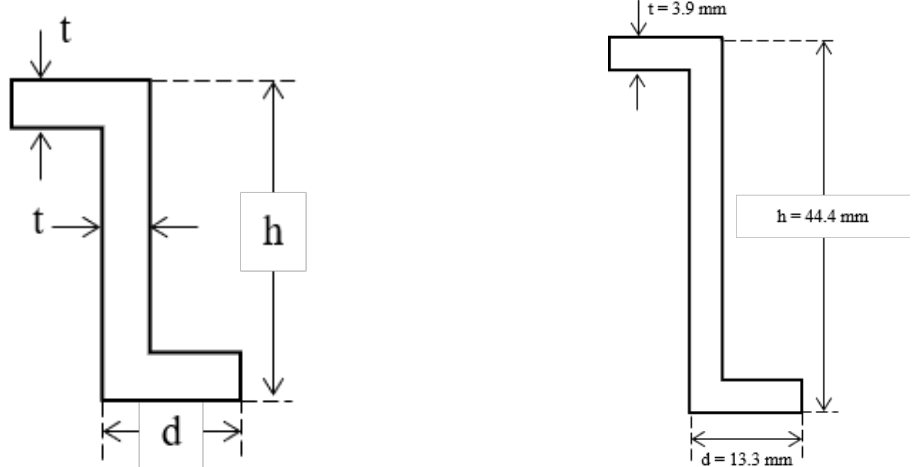
(a) Boom Shear Idealisation

(b) Shear Flow around Fuselage Skin

Figure 30: Boom Shear Idealisation and Shear Flow

A diagram displaying the spacing of stringers can be seen in Figure 30a and a depiction of the direct stresses experienced by each stringer as a result of the bending moment experienced by the aircraft is shown in figure 30b.

Figure 31a defines the dimensional labelling of the Z-stringer and Figure 31b shows our final sizing, which is also summarised in Table 14.



(a) Defining Dimensional Labels of Z-stringer

(b) Final Stringer Dimensions

Figure 31: Z-stringer Dimensions

Table 14: Summary of the Chosen Dimensions for the Stringers

	d (mm)	h (mm)	t (mm)	b(mm)	Area (mm ²)	n
Load Case 1	13.3	44.4	3.9	126	249.4	87

5.4.3 Verification of skin-stringer design

As the fuselage skin carries the bending moment, axial compressions are generated in both the stringers and the skin. Hence, the designed stringer-skin structure should be checked against stringer-skin panel buckling and local plate instability to avoid failure. Equations 41 and 42 were used to evaluate the critical stresses.

$$\sigma_{cr} = \frac{f_{cr}}{f_0} \frac{k\eta_p\pi^2 E}{12(1-\nu^2)} \left(\frac{t}{b}\right)^2 = KE \left(\frac{t}{b}\right)^2 \quad (41)$$

$$\sigma_{cr} = \left(\frac{\sigma_{cr}}{\sigma_0}\right) KE \left(\frac{t}{b}\right)^2 \quad (42)$$

The stress ratios for compression, shear, and bending load types are then calculated by

$$R = \frac{\sigma_{applied}}{\sigma_{critical}} \quad (43)$$

Finally, stress was related to area by Diagonal Curved Web Panels Method introduced in Niu [2]. To avoid failure the stress ratios should be less than 500 mm². Acceptable regions are shown in Figure 32 in the bottom-left areas bounded by the two dash lines. Hence a stringer area of 249.4 mm² satisfied the stability requirement.

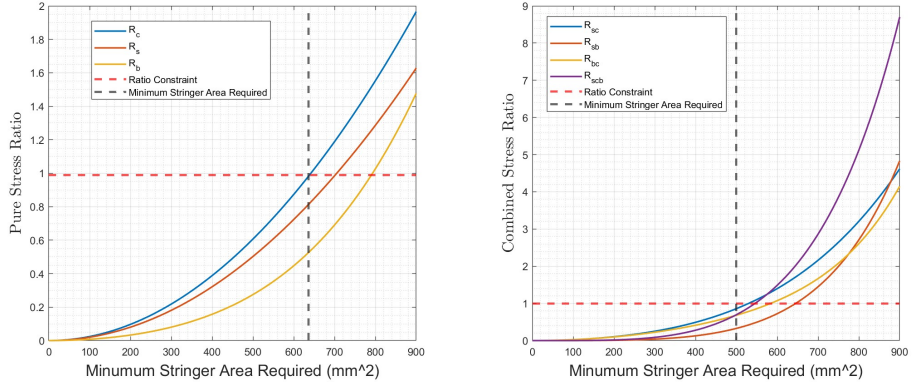


Figure 32: Relationship Between Stress Ratio and Minimum Stringer Area Required

5.5 Light Frame Design

Light frames on the fuselage ensure the general stability of the structure to prevent the complete failure of one of the frames. The following semi-empirical equation in Bruhn [15] was used to size the C-section light frame:

$$(EI)_f = \frac{C_f M D^2}{L_f} \quad (44)$$

where EI is the stiffness of the frame, $C_f = \frac{1}{16000}$ is an empirical constant, D is the diameter of the fuselage, and BM is the bending moment. In most commercial aircraft, the frame spacing L_f is 0.5m. Therefore, it was reasonable to adopt this value in the design as well. Rearrange the above equation, the moment of inertia I_f resisting the bending moment can be expressed as

$$I_f = \frac{C_f M D^2}{E L_f} \quad (45)$$

with I_f being a constant for a specific bending moment. As b was picked to be 0.1016 m (4 inches), the dimensions of the light frame were chosen to adopt a minimum area design. Figure 33 shows the dependency of the frame thickness, height, and width. The final decisions are shown in Table 15

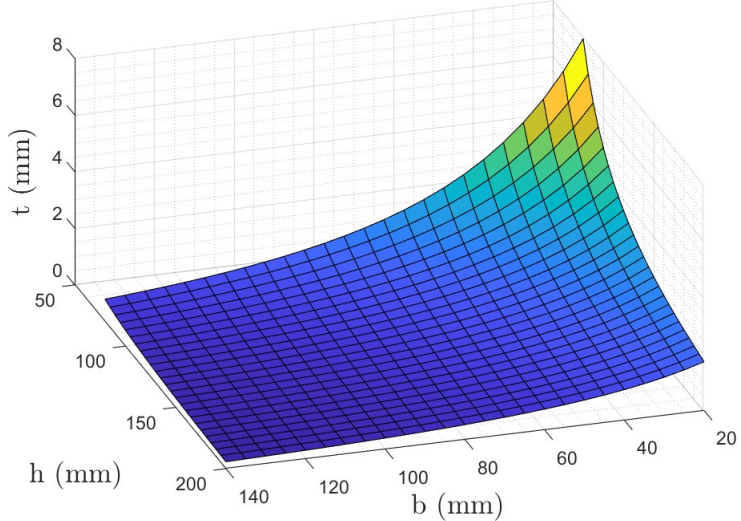


Figure 33: Relationship Between Thickness, Width, and Height of Fuselage Light Frame

Table 15: Light Frame Dimensions

b (mm)	h (mm)	t (mm)	A (mm^2)
100	80	3.2	896

5.6 Heavy Frame Design

Heavy frames are required wherever there is a concentrated load being applied to the fuselage: in this case, at the join of the wing, horizontal tailplane and vertical tailplane struts, as seen in figure (drawing of wehre frames are). In the case of the tailplanes, there are two heavy frames - one for the front spar and one for the rear- while the wing has an additional support for the undercarriage connection.

Initially, a rectangular cross section was considered for the frames; however, this resulted in unreasonably high cross sectional areas and thus was not in line with our weight-saving goal. Instead, an I-section was chosen due to its higher efficiency. The dimensions of the this frame was constrained by one main factor: the space reserved between the fuselage skin and the interior wall decided in the conceptual stage of design, which was chosen to be 9 cm [5]. After many iterations, it was found that this was a much too constraining value, as it resulted in very large bases and thickness compared to height, and so a more reasonable value of 15 cm was decided upon instead.

For the wing and both tailplanes, the point loads being applied to the fuselage were resolved into radial and tangential components and then these, as well as the torque contribution, were used to calculate three load cases: the tangential load case, the radial and the moment load case. The equations for these are displayed in the subsequent subsections, where M_a represents section moment load, N_a the section normal load and S_a the section shear load.

5.6.1 Tangential Load Case

$$M_a = \frac{PR}{2\pi} \left(\frac{3\sin\phi}{2} + (\pi - \phi)(\cos\phi - 1) \right) \quad (46)$$

$$N_a = \frac{P}{2\pi} \left(\frac{\sin\phi}{2} - (\pi - \phi)\cos\phi \right) \quad (47)$$

$$S_a = \frac{P}{2\pi} \left((\pi - \phi)\sin\phi - 1 - \frac{\cos\phi}{2} \right) \quad (48)$$

5.6.2 Radial Load Case

$$M_a = \frac{QR}{2\pi} \left(\frac{\cos\phi}{2} - (\pi - \phi)\sin\phi + 1 \right) \quad (49)$$

$$N_a = \frac{Q}{2\pi} \left(\frac{3\cos\phi}{2} + (\pi - \phi)\sin\phi \right) \quad (50)$$

$$S_a = \frac{Q}{2\pi} \left((\pi - \phi)\cos\phi - \frac{\sin\phi}{2} \right) \quad (51)$$

5.6.3 Moment Load Case

$$M_a = \frac{T}{2\pi}(\pi - 2\sin\phi - \phi) \quad (52)$$

$$N_a = \frac{T}{2\pi R} \left(\frac{3\cos\phi}{2} + (\pi - \phi)\sin\phi \right) \quad (53)$$

$$S_a = \frac{T}{2\pi R}(1 + 2\cos\phi) \quad (54)$$

5.6.4 Superposition of Cases

For each of the elements, the tangential, radial and moment load cases were summed to give the total load experienced by these heavy frames, and the maximum value of direct, shear and bending stresses were calculated, allowing the frames to be sized. The values of Q, R, T and θ for each case is summarised in Table 16. θ is the angle for the point load from the datum, defined as vertically down from the centre of the fuselage. The loads are assumed to act equally on each of the heavy frames for the components.

Table 16: Table displaying values of resolved tangential, radial and moment loads as well as radius and θ . The radius for the horizontal and vertical tailplanes was taken as an average of the radius of the fuselage at the front and rear spars of the component.

	P (kN)	Q(kN)	T (kNm)	R (m)	θ ($^{\circ}$)
Wing	246	610	1.38×10^3	1.75	14
Horizontal Tailplane	1.74	4.79	10.7	1.43	70
Vertical Tailplane	21.5	0.00	5.93	1.49	180

The Wise Diagrams in Figure 34 display the superposition cases for each element of the aircraft.

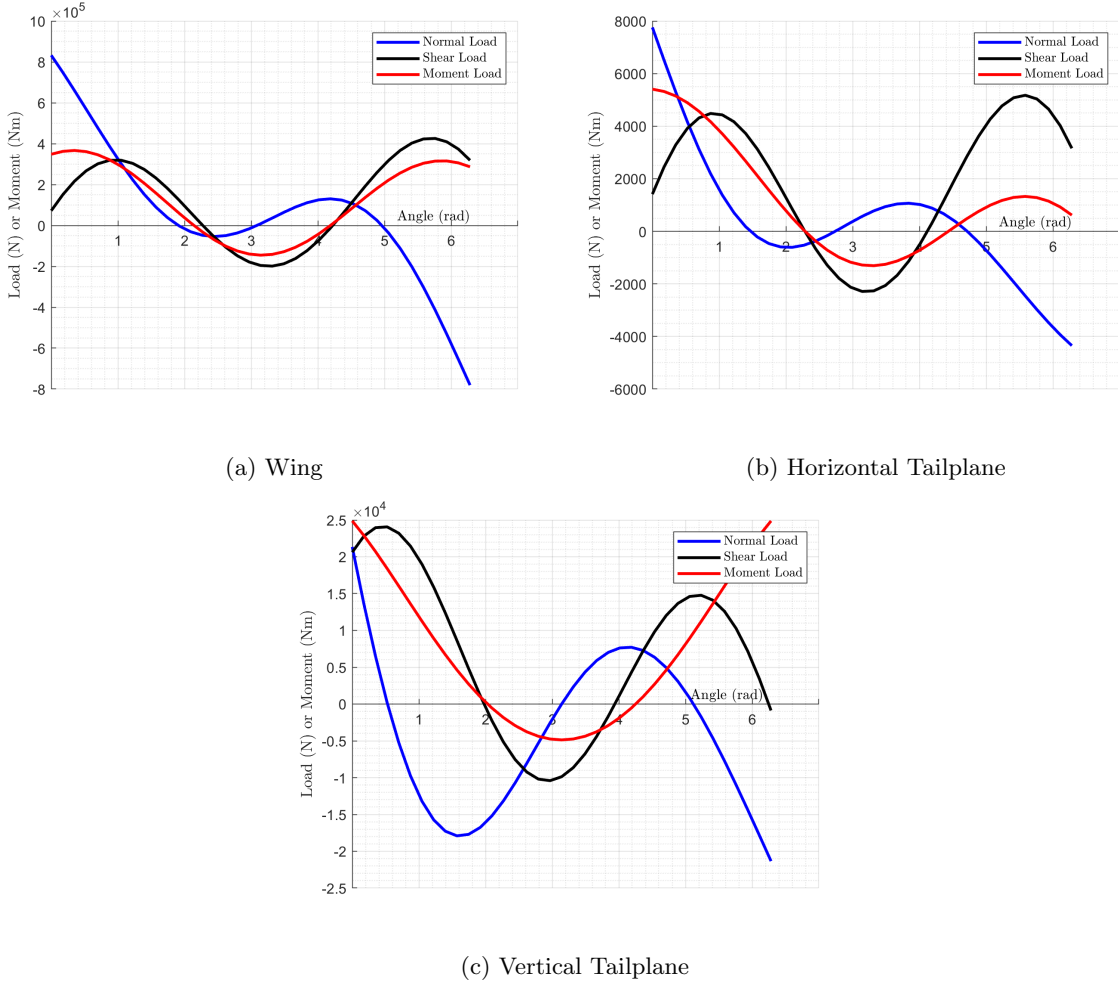


Figure 34: Wise Plots

The actual process of sizing the frames required them to satisfy 2 conditions:

1. The area of the frames is large enough to withstand both direct and shear stresses, defined by equations 55 and 56:

$$A_{shear} = \frac{S_{max}}{\sqrt{3}\sigma_y} \quad (55)$$

$$A_{direct} = \frac{N_{max}}{\sigma_y} \quad (56)$$

The denominator of equation 55 comes from the fact that σ_τ , the tangential stress, can be taken to be a factor of $\sqrt{3}$ the yield stress. The larger of these two areas was taken as the limiting value in each case.

2. The second limiting factor was the second moment of area of the beam: this had to be larger than the second moment of area generated by the bending stress calculated with equation 57. The second moment of area of an I-section can be calculated using equation 58.

$$I_{min} = \frac{M_{max}h}{2\sigma_y} \quad (57)$$

$$I = \frac{th^3}{12} + 2 \left(\frac{bt^3}{12} + t \frac{h^2}{2} \right) \quad (58)$$

In order to calculate the minimum dimensions for the beam, values for b , h and t were iterated and the combinations which satisfied both these conditions were extracted and sorted to determine which dimensions resulted in the minimum area, and thus minimum weight. It was found that the area as defined by equations 56 and 55, summarised in Table 17, was not achievable while also satisfying condition 2, but the dimensions were still within reasonable range.

Table 17: Summary of Minimum Areas Required to Resist Shear and Direct Stresses

	A_{shear}	A_{direct}
Wing	6.86	10.25
Horizontal Tailplane	8.35×10^{-5}	1.51×10^{-4}
Vertical Tailplane	3.88×10^{-4}	6.95×10^{-4}

The defined dimensions are shown in Figure 35, as well as the final dimensions for each of the frames for wing, horizontal tailplane and vertical tailplane. These values are also summarised in Table 18.

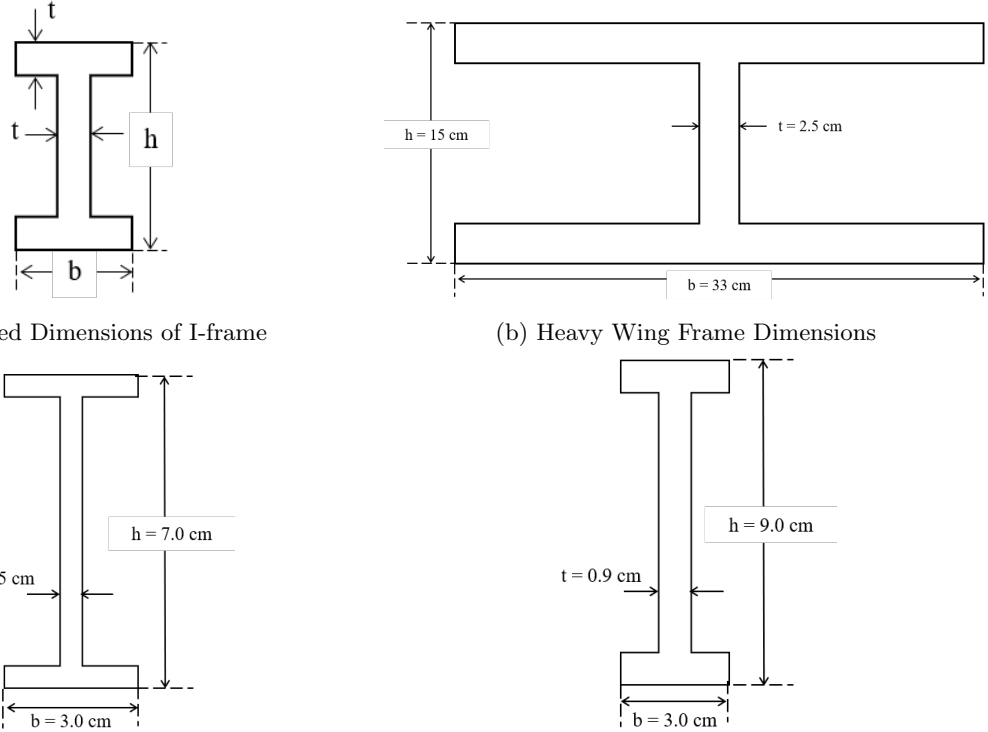


Figure 35: Heavy Frames

Table 18: Summary of Heavy Frame Dimensions

	h (mm)	b (mm)	t (mm)	Area (mm ²)
Wing	150.0	330	25.0	1.9×10^4
Horizontal Tailplane	70.0	30.0	5.0	600
Vertical Tailplane	120.0	40.0	5.0	950

The location of the heavy frame is displayed in Figure 36.

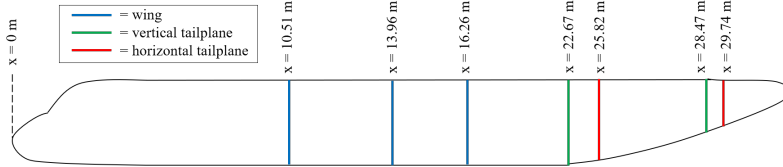


Figure 36: Location of all the Heavy Frames Along the Aircraft

5.7 Mass Breakdown of Fuselage

Table 19: Mass breakdown of Fuselage

Component	Skin	Stringers	Light Frames	Heavy Frames	Total
Mass (kg)	823	1986	1872	1890	6571

This is likely to be an overestimate, as in reality the stringer number would decrease towards the end of the fuselage while in this case it was modelled as a cylinder of constant cross section. For similar reasons, the mass of the fuselage skin is likely to also be an overestimate as taper has not been taken into account.

6 Horizontal Stabiliser Design

The horizontal stabiliser is mainly functioning as the balance for keeping the stability of the aircraft. As it would not be performing as the main lifting surface, the aerodynamic loads applied would be less than that of the wing and so as the inertia loads. The design process would inherit the one in Wing Design, as a similar arrangement of the components would be kept.

6.1 Design Strategy

It was assumed that the bending moment would be resolved into compressive and tensile loads with the same magnitudes in the wing design. This was concluded that an overestimation of the lower skin stringer panels' mass would be expected. This would not be the case for the horizontal stabiliser as it would undertake the bending moment in both directions during the flight. In this design section, the load case for the horizontal stabiliser would be limited to only one load case but the assumption of change in direction of the bending moment would still be valid. The assumption of a rectangular cross-sectional area of the wingbox would be kept and the methodology of structural design would be similar to that of the wing.

6.2 Load Cases

The bending moment, shear force and torque were obtained in a similar way to that mentioned in the wing section. However this time, there was no undercarriage point load, zero lift pitching moment to consider. The final graphs for the bending moment, shear force, and torque can be seen in Figure 37.

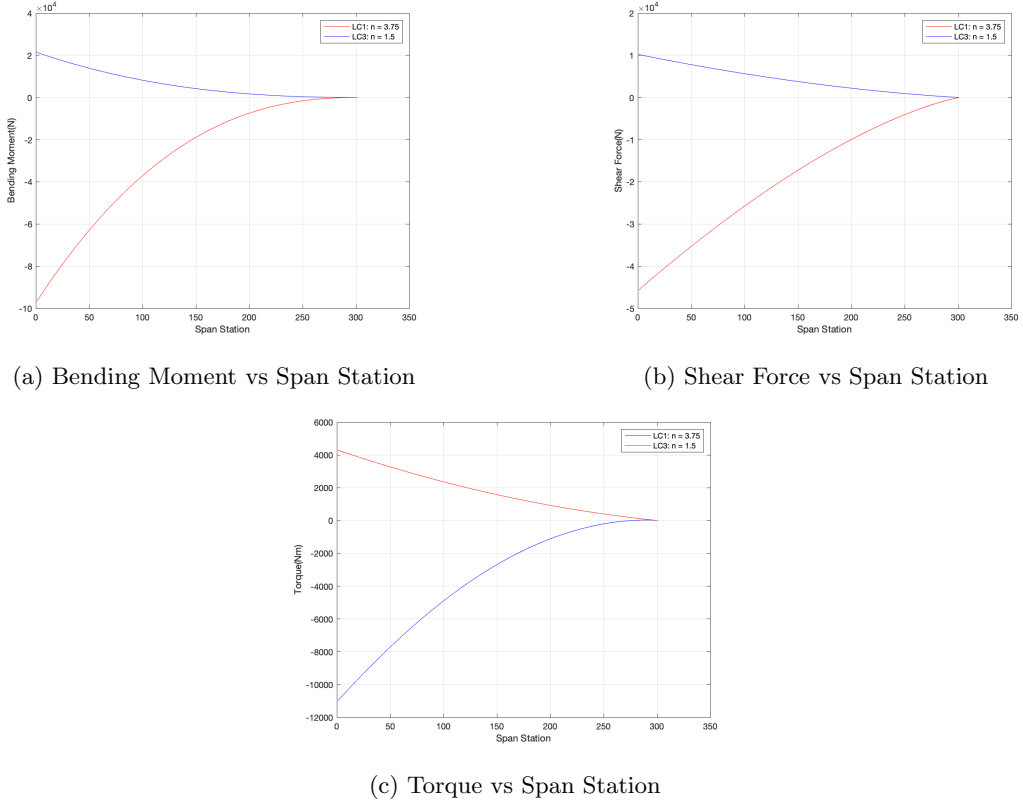


Figure 37: Horizontal tail-plane loads

6.3 Spar Design

6.3.1 Geometry

It was designed that the spar locations would be at 10% and 65% along the chord and the finbox width would be 55% of the chord length [5]. The aerofoil selection was NACA 63-210. The y/c ratios of upper and lower skins at the spar locations are 1.3790%, -1.145%, 4.264% and -2.204% respectively [10]. Table 20 shows the geometry at the root and the tip of the finbox. The worst-case scenario would be considered with the lowest web height which is from the rear spar.

Table 20: Finbox Geometry at the Root and the Tip

Location	Box Width (m)	Rear Spar Height / Web Height (m)
Root	1.96	0.254
Tip	0.588	0.0552

6.3.2 Sizing and Optimisation

With the similar method previously mentioned, the shear flow contributed by the shear force and torque would be calculated, followed by the calculations of thickness and stress. Table 21 shows the dimensions of the first iteration of the spar sizing.

Table 21: Initial Sizing of the Spars at the Root and the Tip of the Wing

Location	Shear Stress (MPa)	Shear Flow (N/mm)	Thickness (mm)
Front Spar Root	21.136	64.985	3.075
Front Spar Tip	0.569	0.134	0.236
Rear Spar Root	21.136	64.984	3.075
Rear Spar Tip	0.568	0.134	0.235

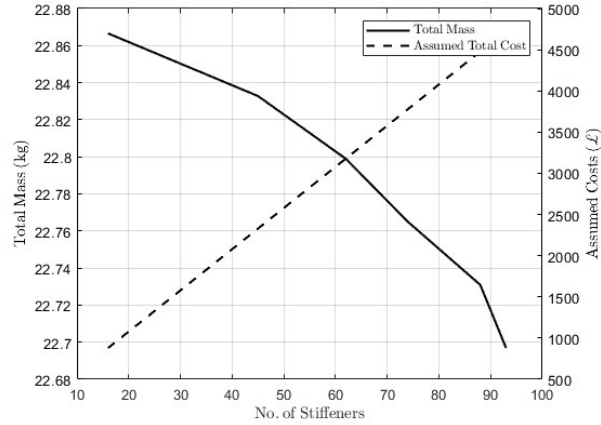


Figure 38: Total Mass and Cost of the Fin Spars Against the Numbers of the Stiffeners

Figure 38 shows the decrease in total mass while an increase in the number of stiffeners attached to the spar. With consideration of the manufacturing cost, the optimum stiffener number would be above 60. The calculation of spanwise spar thickness was made. It is noticed that due to the small magnitude, fewer stages of change in thickness would be modified for manufacturing in comparison with that of the wings. Figure 39a and 39b show the spanwise distribution of spar thickness and Figure 40a and 40b show the stages after modifications.

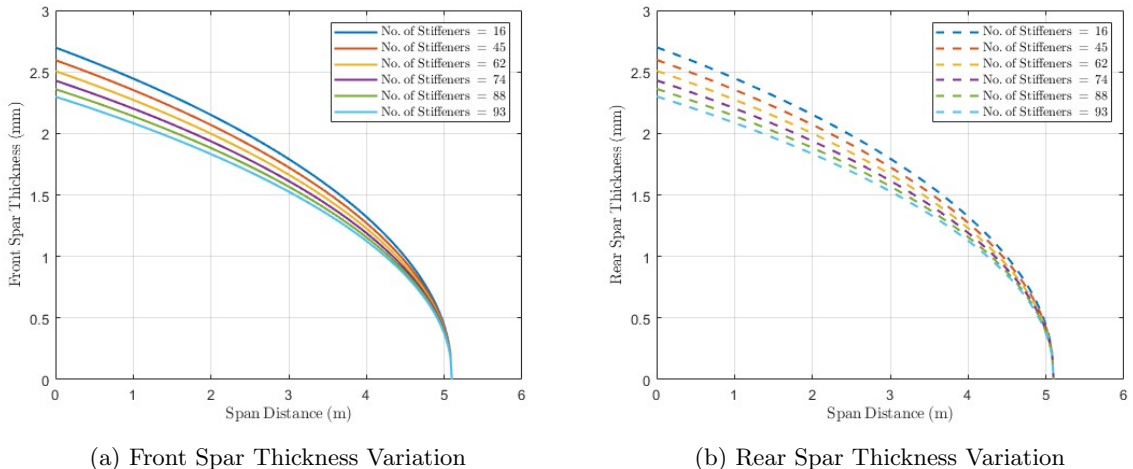
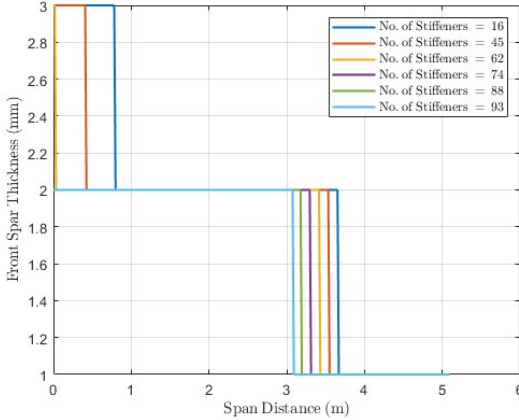
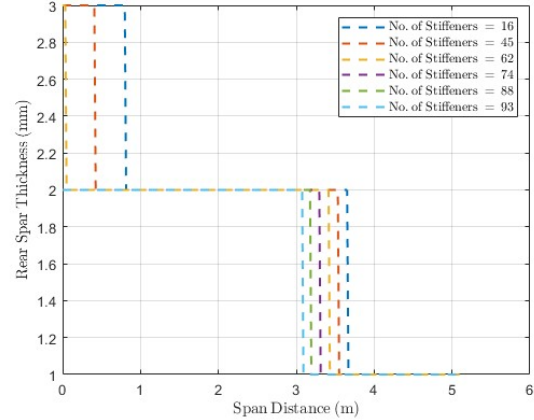


Figure 39: Front and Rear Spar Thickness Distribution Along the Span



(a) Front Spar Thickness Variation



(b) Rear Spar Thickness Variation

Figure 40: Spanwise Thickness Distribution with Manufacture Concerned

6.4 Skin Stringer Panels Design

The Z-section stringers would be applied to the skins and a similar method of fixed ratios would be applied for iteration. By comparison, the optimal $t_{SHT}/t_{HT} = 0.5$ and $A_{SHT}/b_{HT}t_{HT}$ would be used while the corresponding value from Figure 14 would be $K = 1.9$. Figure 41 shows the reduction in mass while increasing the number of panels across the chordwise direction. This was capped by the total expenditure of manufacturing which leads to an optimal number of panels appearing around $n = 50$.

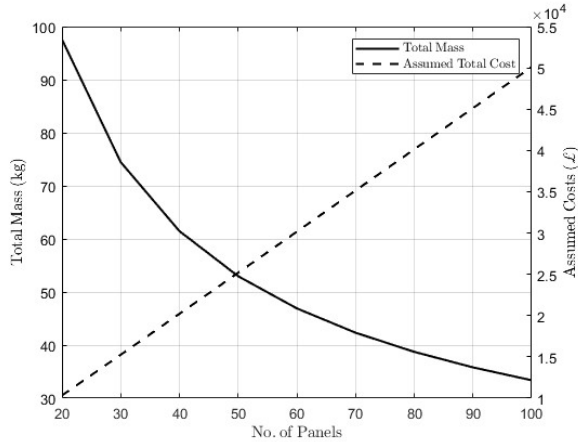
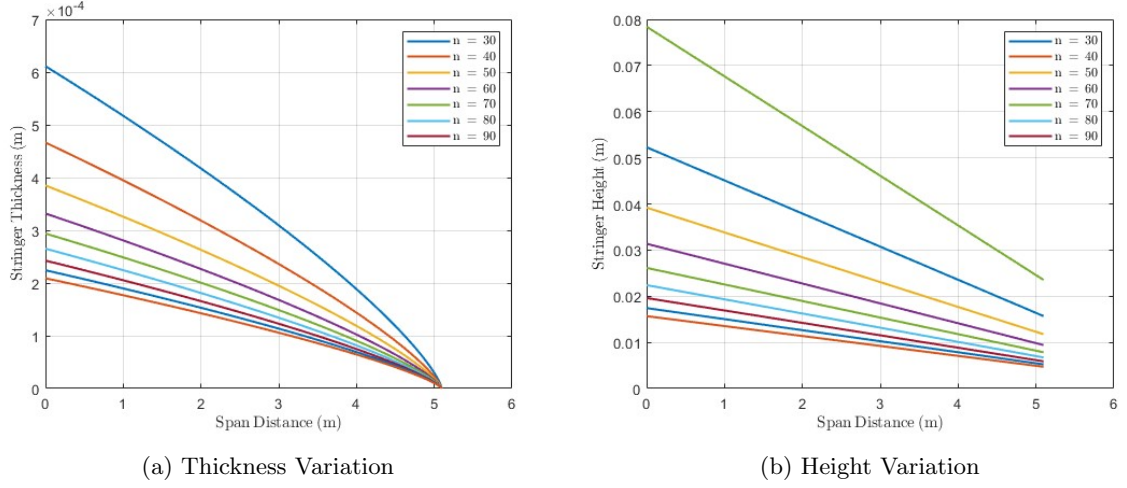


Figure 41: Total Mass and Cost Varies with the No. of Panels

Figure 42a and 42b show the thickness and height variations through the span. As mentioned in previous sections, the tolerance of manufacture would be a concern as the accuracy under 0.1 mm is unnecessary with a dramatic increase in the cost. Figure 43 shows a modification due to this reason. The Farrar factor for the horizontal fins is also considered which would be above 0.7 until close to the tip. The equation 27 was also considered in the fin design while all of the optimised output would satisfy the equation. Detailed digits of skin, stringer and effective thickness at the root and the tip would be concluded in Section 6.7



(a) Thickness Variation

(b) Height Variation

Figure 42: Thickness and Height Distribution Along the Span

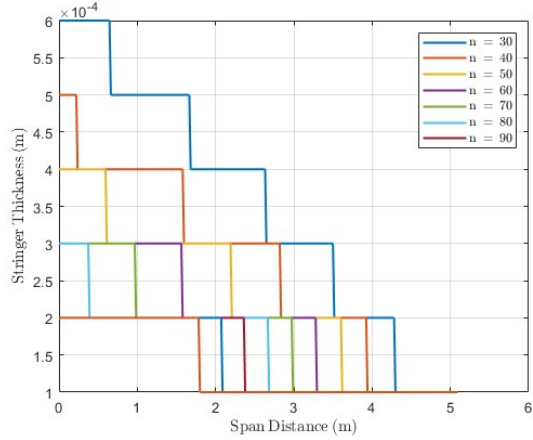


Figure 43: Modification with Clearance and Tolerance Concerns

6.5 Rib design

The rib design for the horizontal tail plane is split in two, which is the design for the main wing box, and the rib design in the leading edge D-cell, which is covered in the next section. It was found that the same study that was done in the wing section was used to design the number of ribs in the horizontal tail-plane wing box.

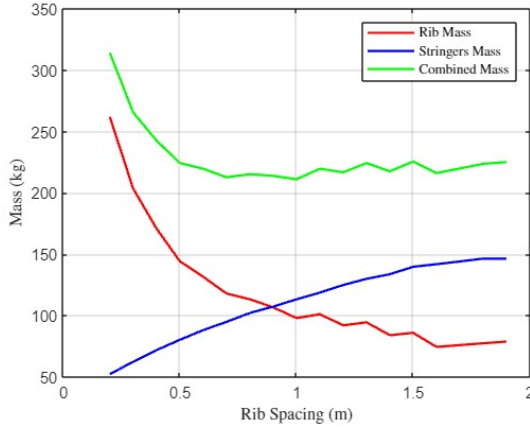
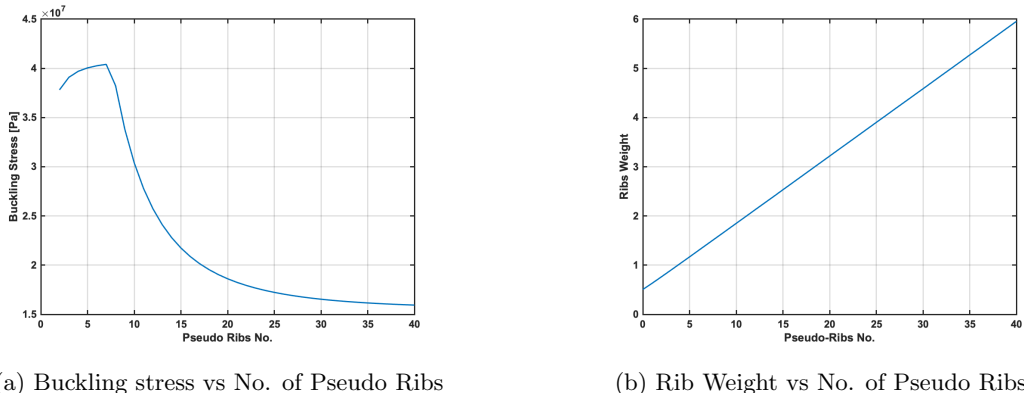


Figure 44: Optimum rib Spacing for Main Wing box of Horizontal Tail-plane

The figure above shows that the best rib spacing was 1.5 mm, giving a total of 5 ribs, as these are the conditions of minimum mass.

6.6 D - Cell section

The D-Cell, which is located at the leading edge of a stabilizer, plays a crucial role in withstanding shear loads. The buckling behavior of the D-Cell under shear loads governs the design of the horizontal stabilizer's D-Cell. It was determined that the best rib structure to be used in the D-cell was the pseudo rib structure. A study was conducted to determine the ideal no. of pseudo-ribs for the horizontal tail-plane. When the number of pseudo ribs was increased with a constant rib spacing, the mass of the tail-plane also increased. As a result, a graph was plotted to compare buckling stress versus the number of pseudo ribs, and it was concluded that seven pseudo ribs were the optimum number. Therefore, a total of seven pseudo ribs were utilized. The trends are observed in Figure 45



(a) Buckling stress vs No. of Pseudo Ribs

(b) Rib Weight vs No. of Pseudo Ribs

Figure 45: Stress and Weight Analyses with Varying Numbers of Ribs

6.7 Geometry & Mass Summary

Table 22: Horizontal Tailplane Rib Geometry Summary with Rib Spacing of 1.5 m

Rib Dimensions 1	2	3	4	5	
Spanwise Position [m]	0.200	0.625	1.050	1.475	1.900
Rib Thickness [mm]	0.0813	0.069	0.055	0.040	0.021

Table 23: Horizontal Tailplane Spar web Geometry at the Root

Spar Web	
Front Spar Thickness [mm]	2.595
Rear Spar Thickness [mm]	2.509
Number of Stiffeners	45

Table 24: Mass Breakdown for the Horizontal Tailplane Components

Component	Skin	Spar	Rib	Total	Estimated Total
Weight [kg]	139.693	22.800	85.833	248.272	300

7 Vertical Stabiliser Design

7.1 Design Rational

As stated in the design brief, one of the empennage structures must be made out of composite and the vertical tailplane was chosen. Due to the anisotropic nature of composites as well as the production of composites that differs from metallic alloys, methods to derive and optimise the tailplane structure would also differ. For the skin, it was a sandwich constriction while the ribs, spars and D-Section was made out of aluminium alloys. Justifications for these choices will be discussed in their respective sections.

7.2 Material Selection

Carbon Fibre Reinforced Polymer (CFRP) was chosen over Glass Fibre Reinforced Polymer (GFRP). One of the largest advantages of CFRP is its superior strength-to-weight ratio over GFRP [16], this results in greater resistance to deflection due to transverse load. This could allow better precision of the tail plane's rudder from the pilot. Additionally, given the aircraft is flying in New Zealand with its warm subtropical climate in the north and cool temperate climates in the south as well as saline conditions from the sea, CFRP's lower coefficient of thermal expansion [17] makes it less likely for it to experience changes in geometry over time and its "Excellent" durability [8] in fresh and sea water makes it the better suited for the environment. While GFRP materials are less expensive than CFRP, the better mechanical properties, fatigue resistance and durability of CFRP make it the better choice.

A well-tested CFRP of IM7/8552 was used. Since the skin was to be of sandwich construction, a foam or honeycomb material was required. The following material index was chosen to find an optimal material.

$$M_{Foam} = \frac{GS_f E^{1/3}}{\rho c} \quad (59)$$

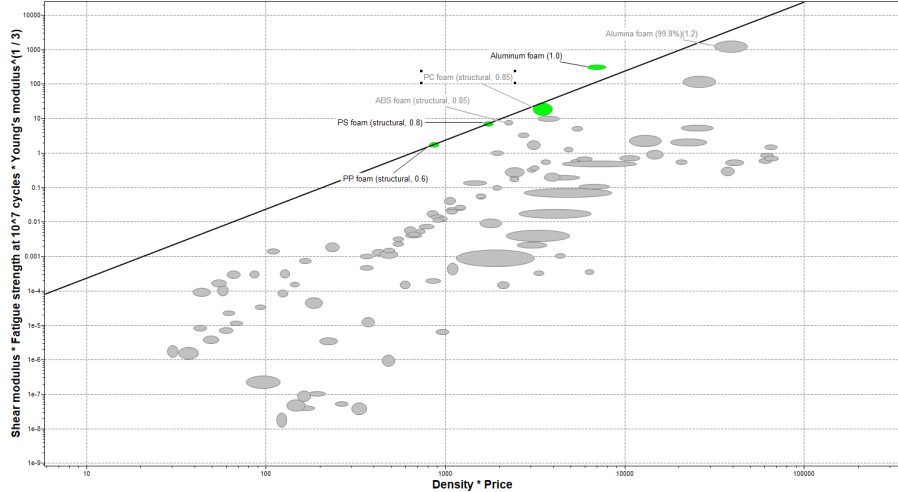


Figure 46: Ashby Chart for M_{Foam} With Design Guideline Slope of 2

From Figure 46 it was clear that Aluminium Foam (Density 1.0) was the optimum choice, however given its difficulty to manufacture and price of £7 per kg [8], it was too complex to bond with the laminates and expensive to be chosen. This left three foams as our core materials with only the PolyCarbonate (PC) Foam ever being used in aerospace components [8].

Table 25: Material Properties for Composite Design. † Tensile Modulus 0° , * In-plane $G_{12} = G_{31}$

	PC Foam	IM7/8552
Density [kg/m ³]	850	1570
Tensile Strength [MPa]	39.5	2720
Compressive Strength [MPa]	1.07	1690
Yield Strength [MPa]	23.5	2720
Young's Modulus [GPa]	1.95	163 †
Shear Modulus [GPa]	0.83	5.17 *
Fracture Toughness [GPa]	1.6	
Poisson Ratio	0.28	0.32
Price [£/kg]	3.84	

7.3 Load Considerations

The methodology for finding the loads acting on the vertical tailplane (VT) was similar to the wings and horizontal tailplane. However, the loads imposed on the VT were calculated by a moment about the aircraft's centre of gravity such that reaction lifting force L_{VT} balanced out the maximum thrust of one engine during the OEI case. The equation was as follows:

$$L_{VT} = T \frac{y_E - y_{CG}}{x_{VT} - x_{CG}} \quad (60)$$

where y_E was the spanwise location of the engine, x_{VT} was the location of the VT longitudinally and T was the maximum thrust produced by one engine. The most limiting case was considered when evaluating the MTOW design of the aircraft since it produced the move aft wards x_{CG} creating the smallest moment arm for the VT to counteract. Unlike the wing or the horizontal tailplane, the vertical tailplane acts vertically down through the structure not perpendicularly to the fuselage, so it was assumed that the internal loading from the weight of the VT was negligible which was further compounded with the composite design of it. Consequently only the shear force, bending moment and torque was considered produced by the lifting force. Out of the three loading cases, the OEI case was the most constraining case imposed onto the VT since it must produce a yaw lift to counteract the thrust coming from the remaining engine, given in Equation 60. Results are summarised in Table 26 and Figure 47

Table 26: Maximum Shear Force, Bending Moment and Torque on the Vertical Tail (at the Root)

Shear Force [N]	Bending Moment [Nm]	Torque [Nm]
5.29E+04	1.27E+05	2.73E+04

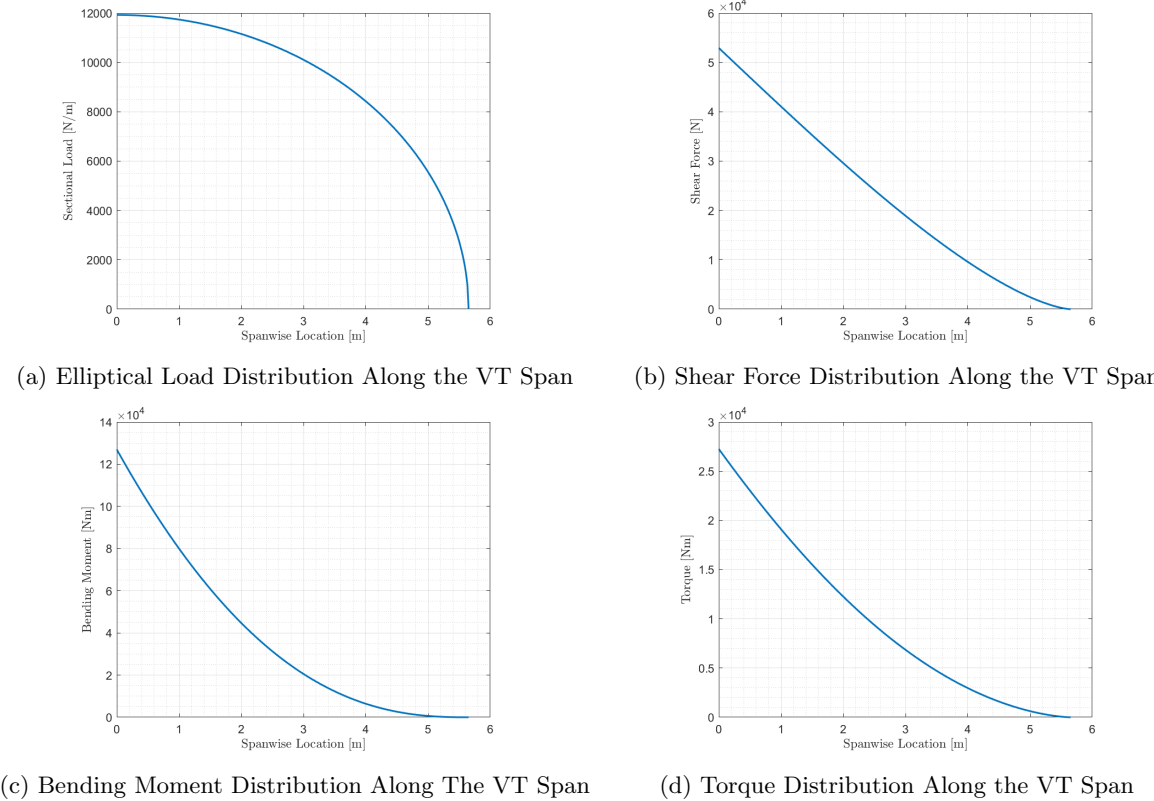


Figure 47: Loads Evaluated in Load Case 2 (MTOW)

7.4 Skin/Cover Design

The vertical tailplane cover, was a sandwich construction. The main reasons to choose a sandwich construction over a composite skin-stringer design were that less composite would be used and the core material was lighter than composites [18]. Furthermore, the core material provided a degree of protection against impact and other types of damage. In the event of damage to one face sheet, the core material can help distribute the load and prevent the damage from spreading [18]. Lastly, sandwich structures would theoretically be easier to manufacture than skin-stringer designs, as they do not require the same level of precision in the fabrication of the stringers, machine tolerance only allows a minimum stringer thickness of 1mm.

7.4.1 Sizing Procedure

The main assumption was that the skin reacts to the bending moment the most, this meant the skin was dominated by 0° plies. Also assuming a nominal ply thickness t of 0.125mm, the number of 0° plies n_{0° to resist the bending moment was calculated using the following equations:

$$N_{xx} = \frac{BM}{hb} \quad (61a)$$

$$n_{0^\circ} = \frac{N_{xx}}{t\sigma_{xx}} \quad (61b)$$

where h was the height of the web, b was the width of the flange and σ_{xx} was the compressive strength of the composite since it was more constraining than the tensile strength. However, the skin might also experience a small amount of shear force as well as transverse forces from foreign objects striking the

skin, therefore the '10% and 70%' [19] was applied to the composite layup to include 45° & 90° plies. The result was two 0° , two 45° and two 90° plies at the root. The initial guess left lots to desire since it would produce an unbalanced laminate and the effect of free-edge interlaminar normal stresses would be greater for such a thin laminate. Doubling the number of plies allowed greater freedom in the ply composition and the stacking sequence of $[0^\circ, 90^\circ, 0^\circ, 45^\circ, 0^\circ, -45^\circ, 0^\circ, 90^\circ, \text{MIDLIN}E]$ was chosen as not only it was symmetrical and balanced but it also kept the interlaminar stresses at the free edge to a minimum, which reduces the likelihood of delamination or layer debonding [20]. The total thickness of the laminate came to 2mm and was constant spanwise to reduce the chance of material failure due to water ingress or temperature changes affecting the air gaps created by the termination points if there was a ply drop-off.

7.4.2 Buckling Analysis

In order to calculate the critical buckling load of the laminate N_{xb}^{cr} , Equation 62 [21], where D_{xx} were obtained from the ABD matrix of the laminate and K_0 was obtained from Figure 70 with $C = 2.0$. The symmetric and balanced composite satisfied the assumptions; it stated that the coupling between bending and extensional deformation could be neglected and there was no bending and twisting deformation [19].

$$N_{xb}^{cr} = \frac{K_0(D_{11}D_{22})^{1/2}}{b^2} + \frac{C\pi^2(D_{12} + 2D_{33})}{b^2} \quad (62)$$

This resulted in the cover buckling under the load for the majority of the spanwise position. The buckling ratio N_{xx}/N_{xb}^{cr} was 117 at the root, this meant either drastically adding more ± 45 plies to resist buckling more [19] or adding a core to the laminate. The latter was chosen as it was the most weight-efficient solution since it would drastically increase the second moment of inertia of the cover making it more buckling-resistant with minimal weight gains. It also allowed the foam thickness to vary spanwise to a greater degree since there was no machine tolerance with foam materials. Therefore, there was no need for ply drop-offs, which decreases the manufacturing complexity and it would prevent any stress concentrations at the termination points causing an increased chance of material failure under cyclic loading [20]. Furthermore, the risk of delamination arising from the interlaminar stress caused by abrupt changes in layer thickness would be minimised during bending. The core material was made out of Polycarbonate foam and was placed at the midline of the laminate layers, after varying the foam thickness and recalculating the ABD matrix to find N_{xb}^{cr} , a foam thickness of 12mm was found at the root which produced a buckling ratio of 0.973, making it suitable. The sandwich layup for the cover was $[0^\circ, 90^\circ, 0^\circ, 45^\circ, 0^\circ, -45^\circ, 0^\circ, 90^\circ, \text{PC Foam (6mm)}, \text{MIDLIN}E]$ at the root and Figure 48 shows the spanwise foam thickness.

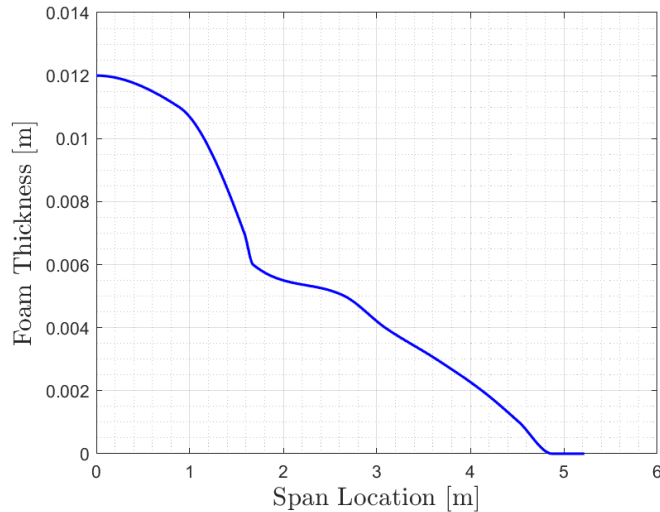


Figure 48: Varying Foam Thickness Spanwise to Increase Buckling Resistance

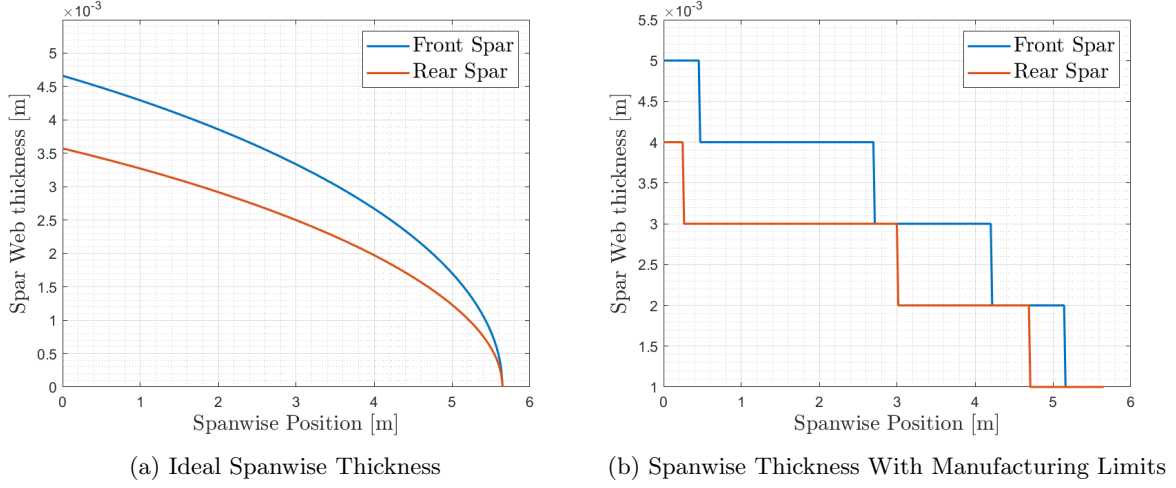


Figure 49: Spar Web Thickness Varying Along the Span of the Vertical Tail

7.5 Spar Design

The initial design of the spar web was also made of composite materials with play drops off spanwise for weight reduction and it was designed with 45° plies dominant in the layup since it resists the shear force the most. From Equation 63, the number of 45° plies was dependent on shear force only; it did not take torque into consideration. If the spar was constructed based on the equations used, it was very likely for the spar to fail due to torsional failure. Therefore, the spar was decided to be constructed with aluminium alloys and the procedure to size the spars for the wings and HT was used for the VT since there were no stringers in the design. Figure 49a & 49b shows the thickness of the front and rear spar in the spanwise direction.

$$N_{xy} = \frac{SF}{h} \quad (63a)$$

$$n_{45^\circ} = \frac{N_{xy}}{t\sigma_{xy}} \quad (63b)$$

To find the number of spar stiffeners, the same procedure for the wing and HT was used. As shown in Figure 50, the optimum number of stiffeners for both spars was 35.

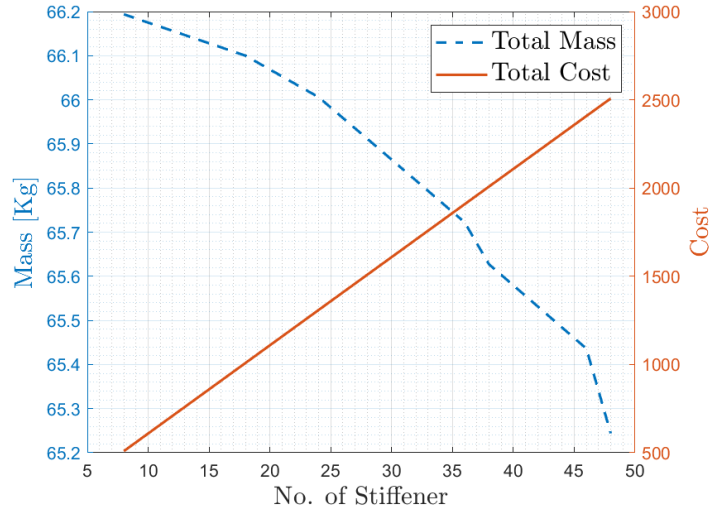


Figure 50: Optimum Number of Spar Stiffeners Using Mass and Cost (in £) Constraints

7.6 Ribs Design

Since the majority of the bending moment loads were taken by the skin and the spar webs were designed to resist the loads from shear force and torque, the ribs were designed with the crushing load when there was deflection in mind. The procedure for sizing the metallic ribs was different to the sizing for the wing and the horizontal counterpart since there were no stingers to consider. But using equation [REF], a plot of weight against rib spacing was produced shown in Figure 51, from it the optimal rib spacing was 2.75m to 4.39m. However, this would mean only one rib spaced closer to the VT tip which was unlikely to maintain the aerodynamic shape of the VT; it could increase the chance of foreign objects striking the VT to leave an impact mark. Re-evaluating the rib spacing, a spacing of 1.5m was considered as a compromise between weight and keeping the aerodynamic shape with 3 ribs. From comparison with the ARJ-21 and A220 previously in Table 1, this decision was validated.

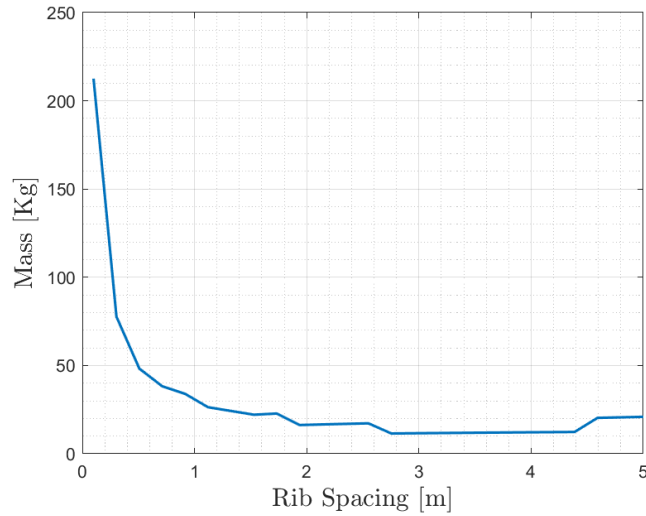


Figure 51: Effect of Varying Rib Spacing on Weight

7.7 D-Section Design

Given that for a composite D-Section, the midline, thus the local neutral axis of the composite would vary around the curvature of the D-Section, analytical analysis between the shear force and the composite was complex. Therefore, it was decided to opt for a metallic D-section as not only would it make analysis easier, but it would also be meant that it would be more durable as the aluminium alloy is more durable and easier to mend than a composite D-Section.

Buckling due to shear loads was the prominent load the D-section was designed to withstand. The design process was much like the horizontal tailplane. The optimisation of the number of pseudo-ribs within the D-section can be found in Figure 52a where it was chosen to make the D-Section skin thickness the same as the tailbox sandwich panel skin. From the figure, it was clear that maximum buckling stress was achieved when there were 3 pseudo-ribs.

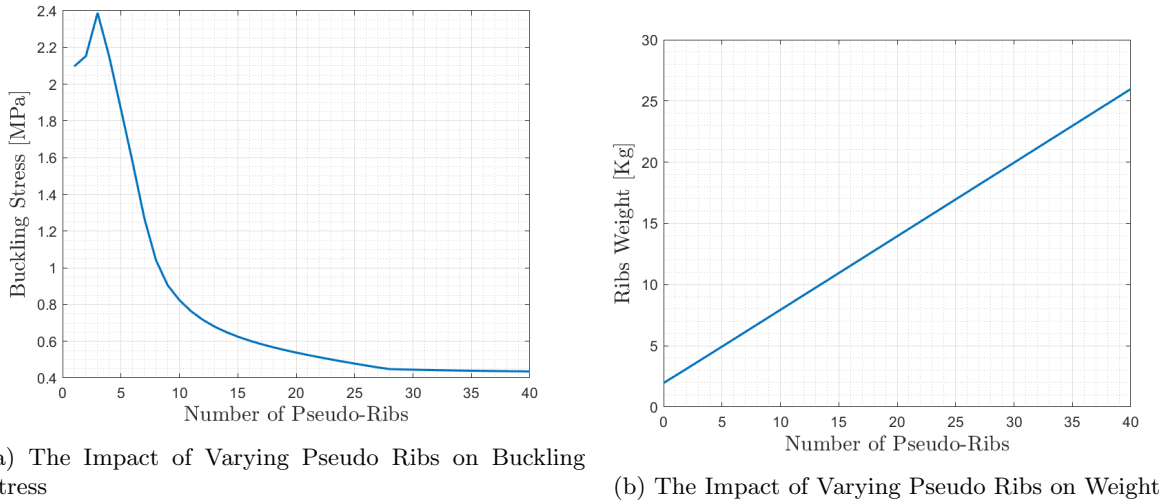


Figure 52: Spar Web Thickness Varying Along the Span of the Vertical Tail

7.8 Geometry & Mass Summary

Table 27: Sandwich Composite Panel Summary With the Thickness Evaluated at the Root

Stacking Sequence	0°	90°	0°	45°	0°	-45°	0°	90°	Foam	MIDLINe
Composite Thickness [mm]									2.00	
Foam Thickness [mm]									12.0	

Table 28: Vertical Tailplane Rib Geometry Summary With Chosen rib Spacing of 1.5m

Rib Dimensions	1	2	3
Spanwise Position [m]	1.50	3.00	4.50
Rib Thickness [mm]	3.00	2.00	1.00

Table 29: Spar web Geometry at the Root

Spar Web	
Front Spar Thickness [mm]	5.00
Rear Spar Thickness [mm]	4.00
Number of Stiffeners	35

Table 30: Mass Breakdown for the Vertical Tailplane Components

Component	Skin	Spar	Rib	D-Section	Total	Estimated Total
Weight [kg]	30.1	94.5	22.4	3.74	150	347

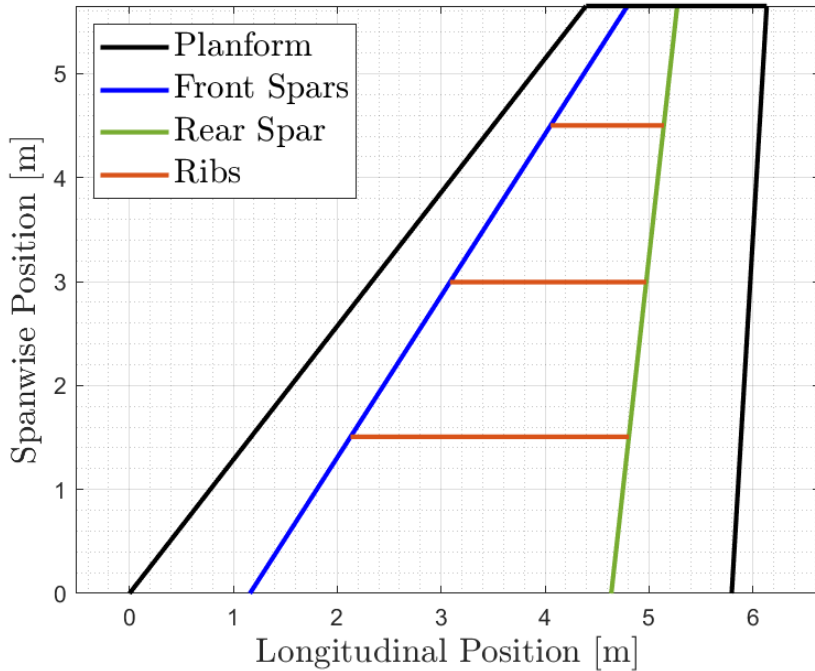


Figure 53: Vertical Stabiliser Geometry

8 Secondary Structures

8.1 Cut-Outs

Cutouts are present throughout the aircraft fuselage as windows, passenger and cargo doors and landing gear deployment mechanism. However, cutout analysis is beyond the scope of preliminary design and these structures can be sized using design principles and comparison with similar aircraft. For unstiffened webs such as the ribs and spar webs, simple lips can be employed to ensure sufficient strength. FE analysis can be conducted on larger cutout such as passenger and cargo doors.

8.2 Joints and Fittings

Joints and fittings must be designed for the aircraft to connect most parts of the aircraft. This is usually outside the scope of the preliminary design phase. However the basic approach, whether welded, bolted or riveted can be considered. For most of the skin stringer connections in the fuselage and the tails, the joints are made using rivets. Clips are also used to attach the ribs and heavy frames for the lifting surfaces and fuselage respectively. This is done while considering a suitable safety factor on the loads applied throughout these structures.

8.3 Engine Mount

The pylon connection between the engine and wing, must be sized to be able to carry the engine loads, while making the joint weak enough to allow it to separate during overload without dangerous damage of the wing. It must also be able to withstand load introductions between the engine and nacelle during normal flight operation by minimising deformations of the engine casing and avoid dangerous resonance vibrations. Thus, the most common way of attaching the engine to the wing is via a pylon box, which itself is attached to the wing structure via an upper and lower strut as shown below.

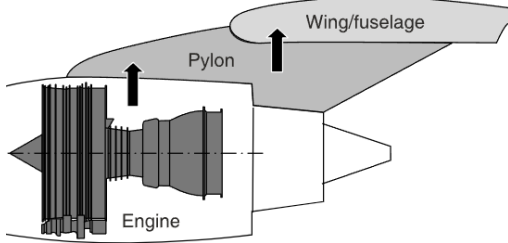


Figure 54: Engine Mount

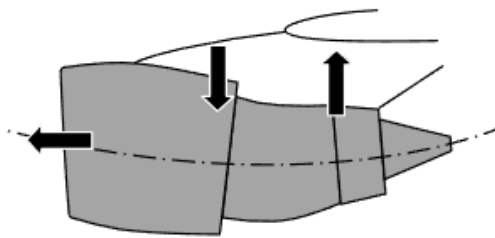


Figure 55: Loading Effects on Engine

8.4 Undercarriage

Similar to the engine, the undercarriage link to the main wing structure should be designed to meet certain breakaway criteria. A tricycle configuration was chosen for the undercarriage for its inherent stability on the ground. As detailed in [5], there are 2 wheels per main undercarriage and nose strut. The two main struts are placed on the wing at 15% of the wing semi-span (to ensure that the engine and main gear are sufficiently far apart) and will fold inwards towards the fuselage, while the nose will fold forwards due to fuselage space constraints.

8.5 Leading and Trailing Edge Devices

The preliminary design phase of an aircraft takes into account the space and attachment points required for both slats and flaps, with the front and rear spars being the respective points of attachment. The design of control surfaces is typically based on their ability to withstand hinge loads and inertial loads, which should be analysed through a more detailed analysis. During the preliminary design phase, it is sufficient to know the placement of these components and the location of the actuators. It is also important to note that impact resistance is less important for secondary structures.

9 Detailed Component Design

The conceptual and preliminary design stage is followed by a detailed design stage whereby the objective is to design and optimise each iteration of a component based on weight minimisation and factors such as buckling, maximum deflection and maximum stress given manufacturing constraints and performance requirements.

9.1 Objective

A component of the flap mechanism, manufactured out of 6082-T6 aluminium alloy needs to be designed, milled and tested. The part is tested structurally through the application of a load at the middle hole. The structure should not deflect more than 5 mm at a LIMIT LOAD of 6 kN and needs to be designed such that an ULTIMATE LOAD = 1.5 x LIMIT LOAD = 9 kN can be applied to it before failure. The main objective of this analysis is to maximise the following merit index η :

$$\eta = \frac{LOAD}{MASS} \quad (64)$$

by minimising the mass of the structure.

9.2 Design Approach and Selection of Final Design

The engineering method used to come up with the final design revolved around an iterative approach. Initially, a static stress and buckling analysis are conducted in ABAQUS on the blank rectangular plate provided as basis [22]. Areas having low stress concentrations were free to be removed, showcasing that the load distribution at these sections were negligible, while areas with higher stress concentrations had to be kept in or have material added around them to mitigate high loading concentrations. This allowed for a new iteration of the design to be conceived with section cutouts in CAD and subsequently the FEA process is repeated on that design. The Von Mises stress was checked during this stage and compared with the Ultimate Tensile Strength of 6082-T6 aluminium alloy, equal to 310 MPa for a wall thickness

> 5 mm [23], making sure that it does not exceed this value. Buckling analysis was similarly conducted to make sure the structure does not buckle and deflect past 5 mm.

In terms of making the design iterations, a few notable factors are considered. Firstly, any abrupt change in geometry such as sharp corners or unnatural shape transitions is eliminated through proper techniques such as adding required fillet radii or arcs where needed or sticking to standard shapes such as triangles similar to a truss structure. This is done while keeping in mind the design constraints of having a minimum internal radius of 4.00 mm and a minimum strut width of 3.50 mm [22]. Following several iterations, in order to minimise mass while still meeting design requirements, it was decided to have most of the mass above the loading pin such that the line of action of the load path is along a larger mass of material above the hole to increase the stiffness in the loading direction, minimising stress concentration around the hole. The extremities of the design were filleted. This is done to minimise the stress concentration factor, given by equation 65:

$$K_t = \frac{\sigma_{max}}{\sigma_{ref}} \quad (65)$$

where σ_{max} and σ_{ref} are the maximum stress and reference set-point stress respectively [24].

In terms of modifying the internal structure of the plate, a truss structure design was opted for initially, knowing that typical Howe truss bridges are considered to have an optimal design to minimise stress concentrations [25]. This allowed for the conception of the following design iterations, considered best in terms of mass optimisation:



Figure 56: Iteration 1



Figure 57: Iteration 2

These had masses of 209.8 g and 214.6 g respectively. However, in terms of stress distribution, these did not meet performance requirement, with iteration 1 having a maximum stress concentration well over the limit of 310 MPa as shown:

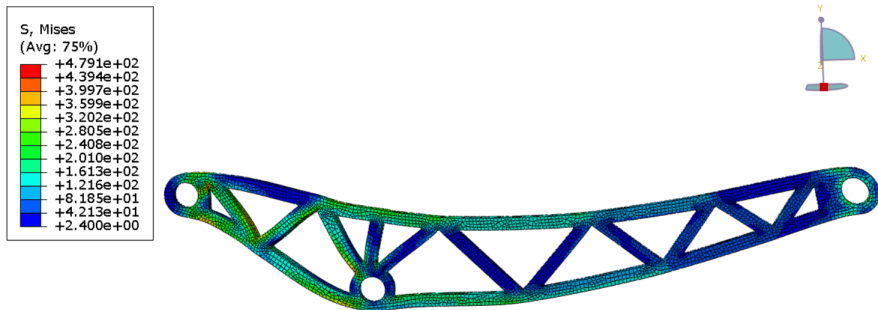


Figure 58: Stress Distribution of Iteration 1

Noting that this stress was concentrated mostly on the left side of the middle hole, this led to the conclusion that premature failure of the structure would ensue if left as is. As such, one improvement made to the design was adding more mass to this side through the inclusion of smaller triangles, leading to the following iterations. The distribution on the right, however, implied that the Howe truss structure would suffice in this segment.



Figure 59: Iteration 3



Figure 60: Iteration 4

This proved successful in reducing the stress while increasing the mass by about 10 %. However, the maximum stress was still well over the 310 MPa benchmark, as showcased by the distribution of iteration 3:

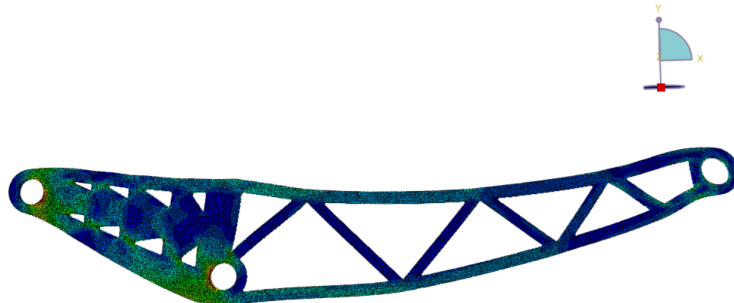
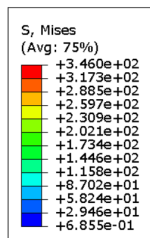


Figure 61: Stress Distribution of Iteration 3

One possible solution explored was increasing the fillet radius on the triangles on the right. However, this made them almost circular, which led to the conclusion that circular cutouts could potentially be used on the left side of the structure to reduce the stress concentration. This is backed by [26], stating that auxiliary holes around a cutout hole can redistribute the stress and potentially reduce it by up to 22 %. This led to several experimental designs having arrangements of holes cutout on the left side, which corroborated the following final iteration, optimised in terms of both mass and performance metrics. Noteworthy is also the fact that the upper side inclination from the leftmost hole was increased to further redistribute and reduce the stress through an increase in mass. The final iteration, despite having a mass of 267.3 g, met all performance requirements as shown by FEA:

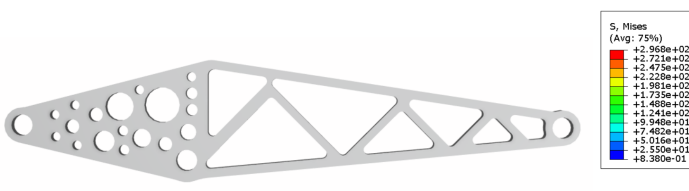


Figure 62: Final Iteration

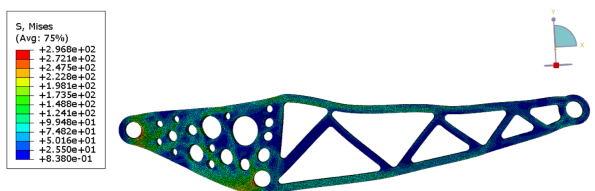


Figure 63: Stress Distribution of Final Iteration

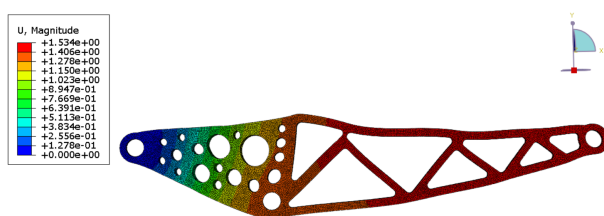


Figure 64: Final Iteration Deflection Magnitude

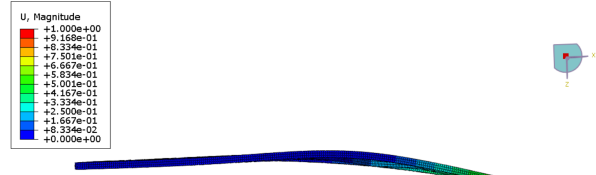


Figure 65: First Buckling mMode of Final Iteration

The selection process for the main types of design variations can be summarised in the table below:

Table 31: Summary of Design Metrics

Iteration	1	3	Final
Mass (g)	209.8	254.8	267.3
Max Von Mises Stress (MPa)	479	346	297
Max Deflection (mm)	3.41	2.64	1.53

9.3 Modelling Assumptions

Based on the problem specification, the leftmost hole is held by a pinned support while the rightmost hole is held by a roller support which is free to move horizontally. These represent the boundary conditions and are modelled as such in ABAQUS. The 9 kN load is made to act on a tie constraint, created based on a reference point at the centre of the middle hole; this ensures the load acts on the entirety of the hole, which might not be the case in real life as there would be a mechanism or pin ensuring the load acts purely at the centre of the hole. This could lead to a slight overestimation of the modelled stress distribution in FEA. Noting that supports are not perfect in reality, an out-of-plane force of 300 N was also included at the middle hole to model potential out-of-plane displacements during the loading phase.

Since this was an iterative process, possibly spanning a range of designs, 2D elements with full integration were used for the mesh generation of the designs to significantly increase runtimes and reduce computational costs, making the optimisation of the design as efficient as possible when going back and forth from FEA to the drawing-board. This involved an assumption of plane stress, but was deemed accurate for finer mesh sizes. The fidelity was further demonstrated through mesh convergence.

9.4 Verification through Mesh Convergence

To validate the accuracy of the FE model, a mesh convergence study is conducted by varying the mesh size for a given run. However, the educational version of ABAQUS is limited to 250000 nodal elements, which limits how fine the mesh can be. This is thus set as a reference setpoint. Starting from a value of 16 mm, the average element size is decreased gradually until the percentage difference in maximum Von Mises Stress between successive meshes is < 5%. The results of this process are summarised below:

Table 32: Mesh Convergence Study

Global seed size (mm)	16	8	4	2	1	0.8
Max Von Mises Stress (MPa)	175	220	267	292	296	297
Percentage Difference (%)	25.7	21.4	7.93	2.41	0.004	0.00

The stress evidently converges to a constant value. This would be shown with greater fidelity had it been possible to use even smaller element sizes. However this is deemed good enough to validate the model.

9.5 Topology Optimisation and Generative Design

Topology optimisation is a mathematical method which spatially optimises the distribution of material within a defined domain [27]. It maximises the performance and efficiency of the design by removing redundant material from areas that do not need to carry significant loads to reduce weight or stress. This allows engineers to optimise a design more effectively knowing which parts can be removed or kept. It is worth noting that topology optimisation, in most cases, produces a design that is often complex or impossible to manufacture. This is due to the fact that the optimisation algorithm focuses on how specific segments of the component transmit loads, attributing a merit index to such sections. Areas with lower indices get trimmed off automatically. For the given task, a rather conservative optimisation was carried out in Fusion 360 in order to avoid overtrimming of the part. As such, the topology-optimised shaped was quite heavy and maintained most of the volume of the original plate. However, in terms of performance metric, the component met all of them, as shown in FE simulation. It thus serves as a guide to indicate redundant parts of the plate that can be removed freely throughout the design process, allowing for greater flexibility in terms of design variety.

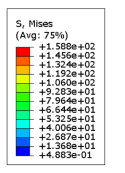


Figure 66: Topology Optimisation Stresses

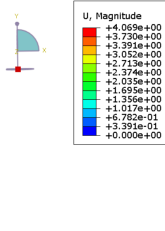


Figure 67: Topology Optimisation Maximum Deflection

In similar fashion, a generative design study was conducted in Fusion 360 by setting up the rectangular plate with required boundary conditions and load as well as specifying geometry to be preserved during the process. Generative design provides a promising algorithmic solution for mass customisation of products, improving both product variety and design efficiency [28]. The generative design employs parameters and goals to quickly explore thousands of design variants to identify the optimal solution, mimicking nature's evolutionary process [29]. Following iterations, the study produces a shape that provides the same insights as topology optimisation albeit much thinner to meet the mass optimisation requirements. However, this design is still not a feasible solution as the shape contains extremely intricate parts that would prove very complex and time-consuming to manufacture. Moreover, when subject to FE simulation, the performance metrics are not met, which suggests that a more conservative approach needs to be taken when designing.

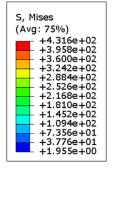


Figure 68: Generative Design Stresses

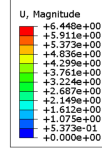


Figure 69: Generative Design Maximum Deflection

The performance metrics and masses of the topology-optimised, generative and final design can be compared as follows:

Table 33: Design Comparison

Design	Mass (g)	Von Mises Stress (MPa)	Maximum deflection (mm)
Final	267.3	297	1.53
Topology-Optimised	880.4	159	4.07
Generative Design	270.6	432	6.45

10 Evaluation of Preliminary Design

10.1 Wing

In the spar design, it was assumed that the stiffeners of the spars are evenly separated. This could be changed with more stiffeners at the root and fewer at the tip, reducing the manufacturing cost. Based on the assumptions made in the skin stringer panels, an overestimation of lower skin mass would be expected. This could be further analysed such as the ratio of how the bending moment would be resolved to the compressive and tensile loads. The flexural centre was assumed located at the centre of the wing box width for this first iteration. After the sizing of all components of the wing, further iterations could be conducted with variations of the flexural axis. A change in rib spacing from the root to the tip could be analysed for reducing mass.

The current total mass is less than the target mass and one of the reasons was the components such

as pipes, slats or other devices were not included. The mass could be aimed to reach the target by generating further iterations.

10.2 Fuselage

Poisson Distribution, originally used in discrete random variables, was used in the mass distribution for some of the aircraft components. For components whose mass was distributed along a larger range of stations, the total cdf could be summed up to reach 1, meaning that the mass of the components had been fully distributed to the stations. However, this was not always possible for components like the horizontal and vertical stabilisers as they had a relatively smaller range to assign, causing a loss in weight assignment, which leads to a slight underestimation of the shear and bending moments.

In this report, the Diagonal Tension Curved Web Method introduced in Niu [2] was only partially applied to relate the stringer and skin areas to stress ratios. Future designs can implement this method fully to take crippling stress into account, allowing for more complicated shape design for the stringers, and could potentially avoid using boom-shear idealisations to achieve for more accurate results.

To give a more accurate design, the heavy frames could be individually sized, as currently it is assumed that the radii of each of the frames are the same and that the load acting on each is the same, which evidently would not be the case in real life. Additionally, the taper could be modelled as this would have a significant impact on stringer spacing and also on the pressurisation modelling of the fuselage. However, as a preliminary design stage, the assumptions made were reasonable to give initial estimates of structures.

10.3 Empennage

Only the cover of the vertical tailplane was comprised of composites while the others were made out of Al 6111-T62. In essence, the vertical tailplane was not entirely made out of composites. The main reason was that sizing for these parts was either too complex like with the D-Section or the procedure for sizing was not like with the spars sizing not including torque load and the procedure for sizing composite ribs was not found. These setbacks would cause negative effects. If moisture or saltwater penetrates the vertical tailplane and was in contact with the composite and aluminium alloy, it could accelerate galvanic corrosion [30]. This would drastically decrease service life and increase-creases the risk of structural faVT's service life and increase ace joining the composite and metallic alloy without an increase in inspections.

A solution to reduce the risk of galvanic corrosion is to use metal like titanium as the joints between the two materials but this would increase the cost. The most ideal solution is to make the VT entirely out of composite and the only point where composite and alloy meet is where the composite spar meets with the metallic fuselage.

The wing box rib design of the entire empennage could be done using a different approach next time, as the same approach as that for the wing ribs was used. This had uncertainties in the sense that the parts of the code used for the wing which was redundant for the empennage had to be substituted, which may not have been a fully accurate model

References

- [1] GROSSMAN N. Elastic stability of simply supported flat rectangular plates under critical combinations of transverse compression and longitudinal bending. *Journal of the Aeronautical Sciences*. 1949;16(5):272-6.
- [2] Niu C. Airframe stress analysis and sizing. AD Adaso/Adastra Engineering LLC; 1997.
- [3] Yang D, Iannucci L. AERO60002 Airframe Design Wing Structural Design;.
- [4] Grihon S, Samuelides M, Merval A, Bruyneel M, Coslon B, et al. Fuselage structure optimization. 2010.
- [5] Yichen Y, Avish M, Stephen C, Aryaa D, Chris Ziyi Y, Amelia S. Conceptual Design Report of a Regional Airliner Jet. Department of Aeronautics; 2022.
- [6] Megson THG. Aircraft structures for engineering students. Butterworth-Heinemann; 2016.
- [7] Traverse P. Airbus and atr system architecture and specification. In: Software diversity in computerized control systems. Springer; 1988. p. 95-104.
- [8] Ashby M. Materials Selection Software CES EduPack. GRANTA; 2023.
- [9] Anderson J. EBOOK: Fundamentals of Aerodynamics (SI units). McGraw hill; 2011.
- [10] Drela M, Youngren H. Aerofoil Tools;. Available from: <http://airfoiltools.com/>.
- [11] Catchpole EJ. The optimum design of compression surfaces having unflanged integral stiffeners. *The Journal of the Royal Aeronautical Society*. 1954;58(527):765â768.
- [12] Levis E. AERO96008 Aerospace Vehicle Design Coursework Briefing Sheet 2022-23;.
- [13] Atmospheric pressure vs. elevation above sea level; 2003. Available from: https://www.engineeringtoolbox.com/air-altitude-pressure-d_462.html.
- [14] Farrar DJ. The design of compression structures for minimum weight. Cambridge University Press; 2016. Available from: <https://www.cambridge.org/core/services/aop-cambridge-core/content/view/8F09BD1D9517954BE97E8B43F155BB58/S0368393100120747a.pdf/the-design-of-compression-structures-for-minimum-weight.pdf>.
- [15] Bruhn EF. Analysis and design of flight vehicle structures. Tri-state offset company; 1965.
- [16] Baker AA. Composite materials for aircraft structures. AIAA; 2004.
- [17] ValeryVasiliev V, Morozov VE. Advanced mechanics of composite materials. the Boulevard, Langford Lane, Kidlington, Oxford. 2007.
- [18] Mouritz AP. Introduction to aerospace materials. Elsevier; 2012.
- [19] Lannucci L. Design for Carbon Fibre Composites. Imperial College London; 2023.
- [20] Agarwal B, Broutman L. Analysis and performance of fiber composites Second edition. John Wiley & Sons; 1990.
- [21] ESDU. Buckling of rectangular specially orthotropic plates.; 1995. Available from: https://www.esdu.com/cgi-bin/ps.pl?sess=unlicensed_1230302113918ppj&t=doc&p=esdu_80023a.
- [22] Errikos L. Aerospace Vehicle Design Coursework Briefing Sheet 2022-2023. Department of Aeronautics; 2022.
- [23] Association A. Aluminum standards and data. Aluminum Association; 2000.
- [24] Kirsch C. Die theorie der elastizitat und die bedurfnisse der festigkeitslehre. Zeitschrift des Vereines Deutscher Ingenieure. 1898;42:797-807.
- [25] Kim SE, Park MH, Choi SH. Practical advanced analysis and design of three-dimensional truss bridges. *Journal of Constructional Steel Research*. 2001;57(8):907-23.
- [26] Jindal U. Reduction of stress concentration around a hole in a uniaxially loaded plate. *The Journal of Strain Analysis for Engineering Design*. 1983;18(2):135-41.
- [27] Gernaey KV, Huusom JK, Gani R. 12th International Symposium on Process Systems Engineering and 25th European Symposium on Computer Aided Process Engineering: Parts A, B and C. Elsevier; 2015.

- [28] Jiang Z, Wen H, Han F, Tang Y, Xiong Y. Data-driven generative design for mass customization: A case study. *Advanced Engineering Informatics*. 2022;54:101786.
- [29] Gupta A, Soni V, Shah D, Lakdawala A. Generative design of main landing gear for a remote-controlled aircraft. *Materials Today: Proceedings*. 2023.
- [30] Yari M. Galvanic Corrosion of Metals Connected to Carbon Fiber Reinforced Polymers — corrosionpedia.com; 2022. [Accessed 03-Mar-2023]. <https://www.corrosionpedia.com/galvanic-corrosion-of-metals-connected-to-carbon-fiber-reinforced-polymers/2/1556>.

Appendix

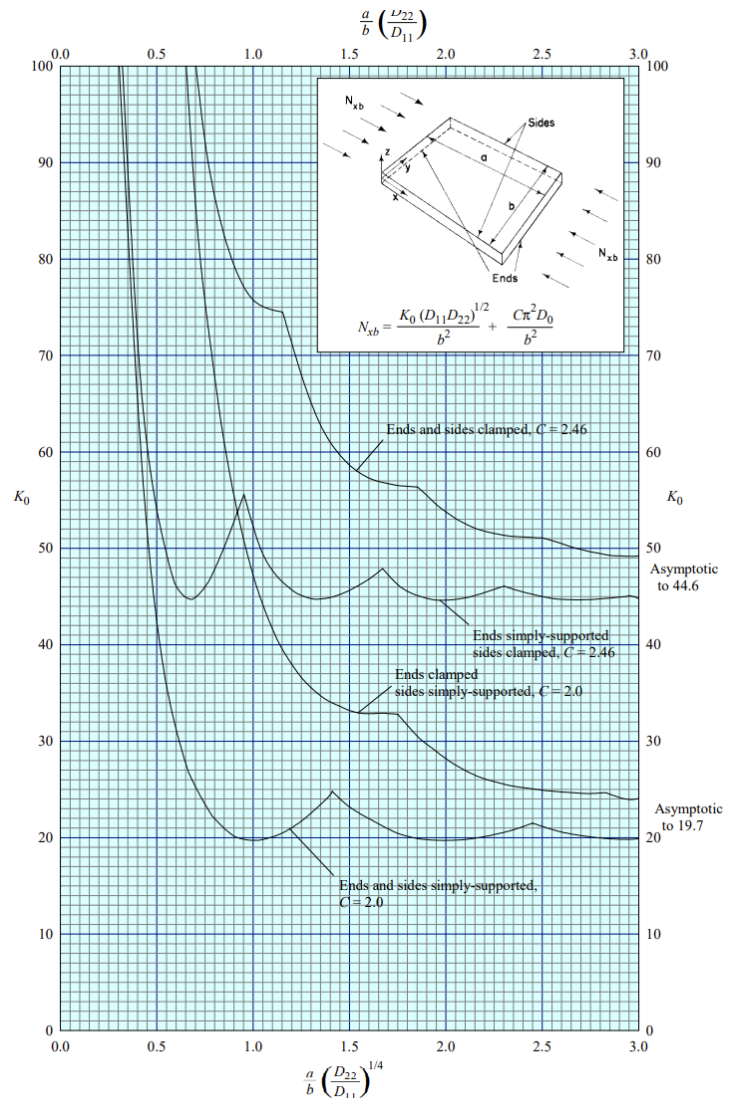


Figure 70: Uniaxial Load Combinations of Clamped and Simply-Supported Edge Conditions